J. Fluid Mech. (2013), *vol.* 721, *pp.* 225–267.
doi:10.1017/jfm.2013.32

Volume displacement effects during bubble entrainment in a travelling vortex ring

Andrew J. Cihonski, Justin R. Finn and Sourabh V. Apte†

School of Mechanical, Industrial and Manufacturing Engineering, Oregon State University, Corvallis, OR 97331, USA

(Received 1 June 2012; revised 14 November 2012; accepted 9 January 2013; first published online 13 March 2013)

When a few bubbles are entrained in a travelling vortex ring, it has been shown that, even at extremely low volume loadings, their presence can significantly affect the structure of the vortex core (Sridhar & Katz, *J. Fluid Mech.*, vol. 397, 1999, pp. 171–202). A typical Euler–Lagrange point-particle model with two-way coupling for this dilute system, wherein the bubbles are assumed subgrid and momentum point sources are used to model their effect on the flow, is shown to be unable to capture accurately the experimental trends of bubble settling location, bubble escape and vortex distortion for a range of bubble parameters and vortex strengths. The bubbles experience significant amounts of drag, lift, added mass, pressure and gravity forces. However, these forces are in balance with each other as the bubbles reach a mean settling location away from the vortex core. The reaction force on the fluid due to the net summation of these forces alone is thus very small and is unable to affect the vortex core. By accounting for fluid volume displacement due to bubble motion, experimental trends on vortex distortion and bubble settling location are captured accurately. The fluid displacement effects are studied by computing various contributions to an effective volume displacement force and are found to be important even at low volume loadings. As the bubble size and hence bubble Reynolds number increase, the bubbles settle further away from the vortex centre and have strong potential for vortex distortion. The net volume displacement force depends on the radial pressure force, the radial settling location of the bubble, as well as the vortex Reynolds number. The resultant of the volume displacement force is found to be roughly at 45° with the vortex travel direction, resulting in wakes directed towards the vortex centre. Finally, a simple modification to the standard point-particle two-way coupling approach is developed wherein the interphase reaction source terms are consistently altered to account for the fluid displacement effects and reactions due to bubble accelerations.

Key words: bubble dynamics, multiphase flow, vortex interactions

1. Introduction

1.1. *Background*

The features of the interaction between vortical structures and bubbles are important in many applications, including microbubble-induced drag reduction in a turbulent

† Email address for correspondence: sva@engr.orst.edu

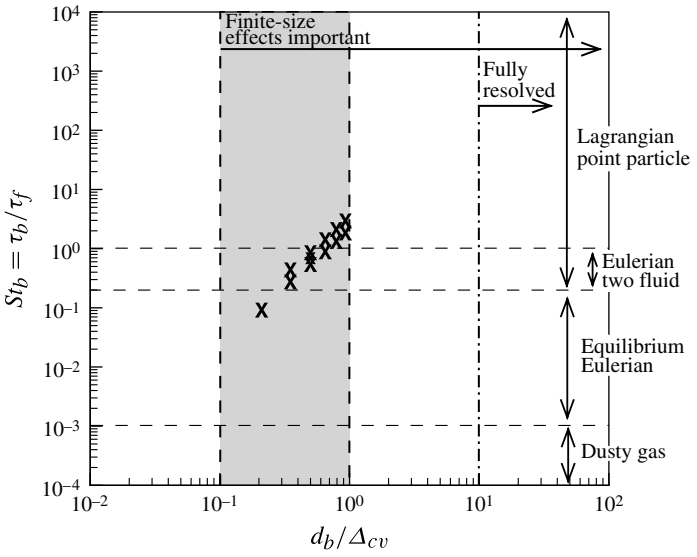

FIGURE 1. A map of the bubble Stokes number versus the non-dimensional bubble size (d_b/Δ_{cv}), modified after Balachandar (2009) and Balachandar & Eaton (2010). The bubble size is non-dimensionalized by the size of the smallest scales of the flow, which are generally proportional to the grid resolution, for example in a direct numerical simulation. Also marked, by X are the cases presented in the present work on bubble–vortex ring interactions.

boundary layer (Ceccio 2010), chemical mixing in bubble column and stirred tank reactors (Sokolichin *et al.* 1997; van der Hoef *et al.* 2008), cavitating tip vortex flows (Hsiao & Chahine 2004) as well as the breakup/coalescence of bubbles in swirl atomizers (Higuera 2004). There is a diverse set of modelling strategies available for simulating dispersed two-phase and bubbly flows. The choice of a particular approach is typically motivated by three parameters emphasized in recent reviews (Balachandar 2009; Balachandar & Eaton 2010), namely, the Stokes number of the dispersed phase, the grid resolution available in the simulation and the bubble volume loading.

Figure 1 is a map, adapted from Balachandar & Eaton (2010), of Stokes number ($St_b = \rho_b \overline{\omega} d_b^2/36\mu_\ell$) versus the ratio of the dispersed-phase (bubble/particle) diameter (d_b) to the smallest flow scales resolved on the computational grid ($\Delta_{cv} = \mathscr{V}_{cv}^{1/3}$, where $\mathscr{V}_{cv}$ is the volume of the computational cell) and the corresponding numerical modelling approaches that can be used. Note that a time scale based on mean vorticity (circulation) is used here, as it is the most physically relevant fluid time scale for vortex-dominated flows. For example, for very low Stokes numbers, the bubbles mainly act as tracers, and a dusty gas ($St_b < 10^{-3}$) or an equilibrium Eulerian approach ($10^{-3} < St_b < 10^{-1}$) (Ferry & Balachandar 2001) is applicable and most efficient. For the range $10^{-1} < St_b < 1$, a two-fluid Eulerian approach (Druzhinin & Elghobashi 1998; Fevrier, Simonin & Squires 2005) is valid, wherein the carrier fluid and the dispersed bubble phases are represented by interpenetrating fluid media, and Eulerian conservation equations are solved for the fluid as well as the dispersed phase together with a concentration evolution equation. Such an approach is advantageous for large numbers of dispersed-phase particles. The Lagrangian point-particle approach (Maxey & Riley 1987; Squires & Eaton 1991) is the most commonly used technique for moderate-sized dispersed phase (up to millions of bubbles/particles) with larger

Stokes numbers ($St_b > 0.1$). In this approach, the dispersed phase is assumed subgrid in scale (smaller than the smallest grid resolution used, with $0.09 \leqslant St_b \leqslant 2.89$ for this work), and particle dynamics equations are solved in a Lagrangian frame. The momentum exchange between the dispersed and continuum phases are modelled as point sources.

The point-particle approach is strictly valid for dispersed particles that are much smaller than the smallest flow scale (for example, the Kolmogorov scale, $\eta \approx \Delta_{cv}$, in turbulent flow, when the fluid flow equations are solved using direct numerical simulation (DNS)). For $d_b/\Delta_{cv} > 0.1$, the finite-size effects of the dispersed particles, such as wakes and mass/volume displacement, become important, and these effects should be accounted for in any modelling strategy. Fully resolved simulation techniques, wherein all length scales and the associated dynamics of the two-phase system are completely resolved on the computational grid, are necessary to capture such effects. However, at least 10 or more grid points in each direction are needed within the particle domain to be able to use this approach. With such high resolution requirements, this approach can be prohibitively expensive for a large number of dispersed particles. In addition, for the regime $0.1 \leqslant d_b/\Delta_{cv} < 10$, one has to rely on subgrid models for the finite-size effects. Under such conditions, the Lagrangian point-particle approach is potentially the only viable approach. This also suggests that it is important to develop less expensive two-fluid and/or Eulerian–Lagrangian models capable of reproducing experimentally observed fundamental physics of bubble-laden turbulent flows. For $d_b/\Delta_{cv} > 10$, finite-size effects are still important; however, the grid is sufficiently resolved to capture these effects without requiring any additional models. This is important not just for simulations of small-scale bubble–fluid interactions, but also for the development of closures for higher-order models based on the Reynolds-averaged Navier–Stokes equations. Of particular interest are methods for handling bubbles whose size is near that of the smallest resolved fluid scales ($0.1 \leqslant d_b/\Delta_{cv} \leqslant 1$). Around this scale, individual particles/bubbles are large enough to displace a significant amount of fluid mass as they move, but are too small to be modelled with any sort of resolved approach.

There are several ways to implement Lagrangian point-particle models for disperse multiphase systems (Elghobashi 1991). The three traditional methods are known as: (i) one-way coupling; (ii) two-way coupling; and (iii) four-way coupling. A series of works aimed at classifying the dominant mechanisms in particle-laden isotropic turbulence have been performed (Elghobashi 1991, 1994, 2006), which led to the development of a map relating the particle Stokes number and system volume fraction (ϕ) to the dominant mechanisms of interphase momentum transport. While the current work focuses on bubbles, the maps developed in this series of papers should be generally valid for interface-contaminated bubbles of the same Stokes numbers as the particles. Figure 2 shows this map, adapted from Elghobashi (2006), which is designed to reflect the dominant effects on the global flow structures, not necessarily local transient effects.

In one-way coupling, the fluid phase moves the disperse phase, but the reaction force of the particles onto the fluid is considered negligible. In general, this approximation is considered valid when both the volume loading and Stokes number of the dispersed phase are small, in other words, when the disperse phase is expected to have minimal influence on carrier phase motion. The majority of studies based on the Lagrangian point-particle approach for practical applications utilize a two-way coupling method, in which the disperse phase is modelled as a collection of point sources in the carrier fluid momentum equation. For example, several simulations

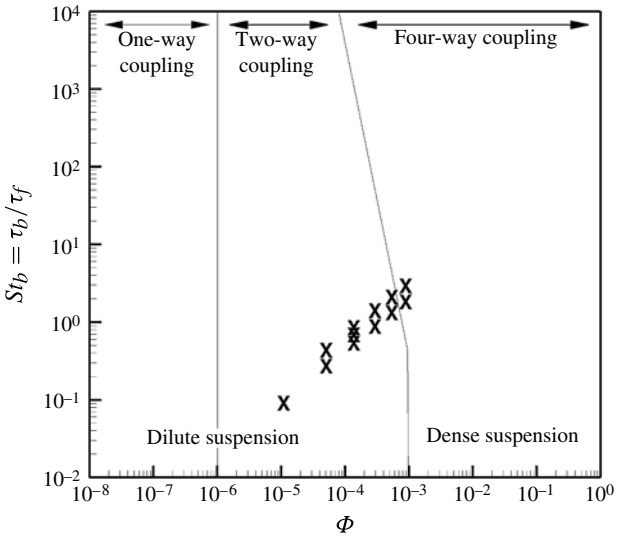

FIGURE 2. Map of Stokes number versus volume loading, modified based on Elghobashi (2006), identifying different momentum transfer modelling approaches applicable for particle-laden flows. The cases presented in this work are marked with an X.

of particle-laden flows have been performed with the carrier fluid simulated using direct numerical simulation (Reade & Collins 2000; Armenio & Fiorotto 2001; Li *et al.* 2001; Rouson & Eaton 2001; Xu, Maxey & Karniadakis 2002; Vreman 2007; Mazzitelli & Lohse 2009), large-eddy simulation (Wang & Squires 1996; Apte *et al.* 2003; Segura, Eaton & Oefelein 2004; Moin & Apte 2006), or Reynolds-averaged Navier–Stokes equations (Sommerfeld, Ando & Wennerberg 1992; Sommerfeld & Qiu 1993).

The two-way coupling approximation is valid when inter-phase momentum transport is dominated by the drag between individual elements of the dispersed phase and collisions between the dispersed phase do not alter the momentum transfer significantly. For dense suspensions (large volume loadings), however, inter-particle collisions must be accounted for in addition to the two-way coupling effects, in a model termed four-way coupling. Four-way coupling can be important even under some moderate loadings, such as the particle-laden jet studied by Lain & Garcia (2006) or turbulent channel flows investigated by Yamamoto *et al.* (2001), and are necessary for applications involving fluidized beds and bubble-column reactors (van der Hoef *et al.* 2008).

The aforementioned coupling methods typically neglect the fact that locally the dispersed phase can displace fluid mass. In many systems, these effects may be unimportant, such as an air pipe flow laden with copper beads (Vreman 2007), where the drag from the two-way reaction coupling force is the dominant mechanism of momentum exchange. For many densely loaded systems, the fluid mass displacement effects are accounted for as part of the four-way coupling formulation, for example, bubble–liquid interactions in column mixers (Sokolichin *et al.* 1997), rising bubble columns (Shams, Finn & Apte 2011) and boundary layer drag reduction (Ferrante & Elghobashi 2005, 2007*a*), among others. Two-fluid formulations implicitly include these effects, through local variations in dispersed-phase concentration (Druzhinin &

Elghobashi 1998; Ferrante & Elghobashi 2007*b*), owing to the assumption that these effects are only dominant when the dispersed-phase volume fraction is significant.

In the present work, it is hypothesized that the local fluid mass (or volume) displacement effects are important even under dilute loadings, especially for lighter-than-fluid dispersed bubbly flows (Finn, Shams & Apte 2011; Shams *et al.* 2011) or particle–fluid systems with small specific gravity such as sediment flows (Apte, Mahesh & Lundgren 2008), wherein the two-way interaction force can be very small. In order to distinguish these effects from the standard momentum coupling techniques described above, we refer to this model as *volumetric coupling* in this work. The main hypotheses that are central to this work are as follows:

(*a*) For subgrid but large dispersed bubbles ($0.1 < d_b/\Delta_{cv} < 1$), a point-particle Lagrangian approach, with standard two-way interphase momentum coupling, may be insufficient to capture accurately the effect of the bubbles on the fluid flow.

(*b*) The fluid volume displacement effects associated with the motion of the bubbles, as well as due to local clustering, are important and should be accounted for to appropriately capture the effect of the bubbles on the fluid flow, even for low volume loadings.

A major objective of this paper is to show that bubble-laden flows in this regime can be effectively modelled using an Eulerian–Lagrangian approach that accounts for the volume displacement effects of the bubbles. In order to test these hypotheses, a test case of a travelling vortex ring laden with a small number of microbubbles is considered, as detailed experimental data are available (Sridhar & Katz 1999). Experimental evidence from this configuration suggests that, under certain conditions, a few small bubbles, corresponding to the conditions marked by an X in figures 1 and 2, can drastically alter local flow structures. In the map, the bubble Stokes number is obtained as $St_b = \tau_b/\tau_f = \rho_b \overline{\omega} d_b^2/36\mu_\ell$, where $\tau_b = \rho_b d_b^2/36\mu_\ell$ is the bubble response time scale, $\tau_f = 1/\overline{\omega}$ is the small feature fluid time scale, $\overline{\omega}$ is the mean local vorticity, d_b is the bubble diameter and μ_ℓ is the dynamic viscosity. These maps indicate that a two-way coupling Lagrangian point-particle approach is appropriate for this problem. However, it will be shown that solely utilizing the two-way momentum coupling methods is not sufficient to reproduce the experimental observations. It should also be noted that the cases studied fall in the range of $0.1 < d_b/\Delta_{cv} < 1$ (figure 1), for which the standard Lagrangian point-source approximation is not strictly valid; however, performing fully resolved simulations is prohibitively expensive.

1.2. *Vortex–bubble interaction*

The interaction of bubbles with vortical flow features serves as an important canonical problem to advance our basic understanding of more complex flows where such flow structures are common, such as turbulent, separated or wall-bounded flows, and has been studied extensively. Oweis *et al.* (2005) studied the properties of bubble capture and cavitation in a line vortex. Their study utilized a one-way coupling approach to predict capture times, which was found to be accurate when utilized for small bubbles, but was not sufficient when bubble growth was a significant factor. Sridhar & Katz (1995), Van Nierop *et al.* (2007), Bluemink *et al.* (2009) and Rastello, Marié & Lance (2011) utilized experimental methods to determine empirical correlations for drag and lift coefficients on bubbles in vortical structures. In studying these lift and drag coefficients, Sridhar & Katz (1995) found significantly higher lift coefficients than were present in many previous studies and suggest that an appropriate choice of drag model is very important within an isolated vortical structure to correctly

predict bubble behaviour. Two-way coupling of bubble interactions with homogeneous isotropic turbulence was investigated by Mazzitelli, Lohse & Toschi (2003). They concluded that bubble accumulation on the downward side of vortices was primarily due to the lift force, in what is known as the preferential sweeping mechanism. Deng, Wang & Smith (2006) experimentally investigated the behaviour of bubbles in a Taylor vortex wherein the drag and buoyancy forces are in balance, in line with later observation in this work. Lohse & Prosperetti (2003) studied the equilibrium position of a bubble in a horizontally rotating cylinder and suggested the need for future studies investigating different lift models.

Sridhar & Katz (1999) showed that a few low-Stokes-number bubbles have the ability to augment the core structure of both laminar and turbulent travelling vortex rings during their entrainment cycle. This is significant, owing to the extremely low overall volume fraction in comparison with the magnitude of the core distortion observed. The case of bubble entrainment into a travelling vortex ring was chosen to test the ability of the volumetric coupling approach to predict the experimental trends for this low-volume-loading case. This case is also ideally suited to identify the effects of volume displacement, as the bubbles tend to settle in a small region away from the ring centre, where all the forces on the bubbles are in balance. The effect of any point-source reaction force on the flow structure is thus generally small.

Recently, Finn *et al.* (2011) investigated a two-dimensional generalization of this problem, by studying a travelling vortex tube laden with a few microbubbles, wherein a periodic boundary condition was used in the direction of the vorticity vector. With dilute bubble volume loadings ($<10^{-2}$), the volume displacement effects due to bubble motion were found to be significant. Results from that work suggested that, for the two-dimensional vortex tube, there was a decrease in the local vorticity at the core centre and volume displacement effects were necessary for significant vortex distortion to occur. However, periodicity in the spanwise direction implied that there are several bubbles in the plane normal to the propagation of the vortex tube. In this work, it will be verified that, even in a three-dimensional vortex-ring configuration, these effects are dominant in comparison to two-way coupling momentum transport. The concept of a *volume displacement force*, the force induced on the liquid due to volume displacement effects, will be developed and compared with the standard two-way coupling force to evaluate their relative magnitudes. The goal of the present work is not only to show that the volumetric coupling effects are important to predict the experimentally observed trends for the bubble-laden travelling vortex ring, but also to study the fundamental nature of the bubble–vortex interactions and explain some of the trends observed by performing various parametric studies. The following key contributions of this work can be identified.

(*a*) The previous work (Finn *et al.* 2011) was a two-dimensional study and the present work is a full three-dimensional study. Although this in itself is a significant difference in the actual problem setting, this work also focuses on several new aspects of the bubble–vortex ring interactions and helps explore fundamental physics of this interaction by using two-phase flow modelling. Note that the two-dimensional study involving a travelling vortex tube has periodic conditions in the spanwise direction, resulting in periodic volume loading and thus increasing the overall volume loading compared to a full three-dimensional domain where only eight bubbles are injected in the whole domain. In addition, the overall computational difficulty associated with unsteady, three-dimensional flows is significantly larger than the two-dimensional counterpart.

(*b*) The comparison of the two-way and volumetric coupling formulations is part of the previous work as well; however, in the present work, a method of measuring and analysing volume displacement effects is introduced, which relies on the notion of the volumetric reaction force (§ 2). Previously, these forces were obtained by mapping the vortex flow onto a simple two-dimensional Gaussian vortex model. However, in the present work, the various mechanisms that contribute to the volumetric reaction force are explicitly determined by directly evaluating each term in the volumetric coupling model. These force contributions are analysed in detail and they also show key differences when compared with the simplified two-dimensional Gaussian vortex estimate. This work demonstrates that, for a full three-dimensional system, the volume displacement forces are significantly larger than the point-particle momentum coupling forces. This detailed force analysis also facilitates computation of the direction of the net force on the fluid due to the presence of bubbles, which correlates well with the direction of the vortex distortion observed in the present work as well as in the experiments.

(*c*) The present three-dimensional work also facilitates direct comparison with the experimental data of Sridhar & Katz (1999), and helps to explain the mechanisms of vortex distortion by a few micrometre-sized bubbles through a wide range of parametric studies. For example, it is argued that the volumetric coupling model captures the wake effects produced behind the bubbles that are essentially not captured by the standard point-particle approach. The present work, through scaling analysis, shows that the vortex distortion due to bubbles is dependent on the bubble settling location as well as the vortex Reynolds number. Although the bubble settling locations are mainly governed by the buoyancy (bubble size) and pressure-gradient (vortex strength) effects, the present work shows that, in order to predict the distortion of the vortex due to bubbles, the vortex Reynolds number also plays an important role. It is shown that the non-dimensionalized net volumetric displacement force is dependent on the bubble settling location ($\bar{r}_s$) and the square of the vortex Reynolds number.

(*d*) Finally, a novel simplified mathematical model that modifies the standard two-way coupling interaction force to include the volumetric displacement effects is formulated. The model can be used in any Euler–Lagrange computation, without the need for significant changes in the numerical algorithm that accounts for local changes in bubble void fractions. The model is consistent, in the sense that, in the limit of extremely small volume loadings $\theta_\ell \to 1$, it reverts to the standard point-particle two-way coupling approach.

1.3. *Problem description*

A travelling vortex ring, shown in figure 3(*a*), is generated through an inlet velocity pulse (Sridhar & Katz 1999; Finn *et al.* 2011). This pulse forms a shear layer, which rolls up into a vortex ring that is convected downstream. At 0.5 m downstream from the inlet, the vortex ring is fully developed, at which point bubbles are injected individually every 10 ms just in front of and below the bottom portion of the ring. The bubbles then begin the entrainment process, in which they circle the lowest portion of the ring to arrive in front of the vortex core centre, as shown in figure 3(*b*). Once the entrainment process is complete, the bubbles tend to settle around a mean location, referred to as the bubble settling location, with coordinates (r_s, θ_s) defined with respect to the core centre. At the settling location, the forces on the bubble are nearly in balance, i.e. sum close to zero in each direction. The force balance on the bubbles at a radial settling location from the core, shown in figure 3(*c*), indicates a

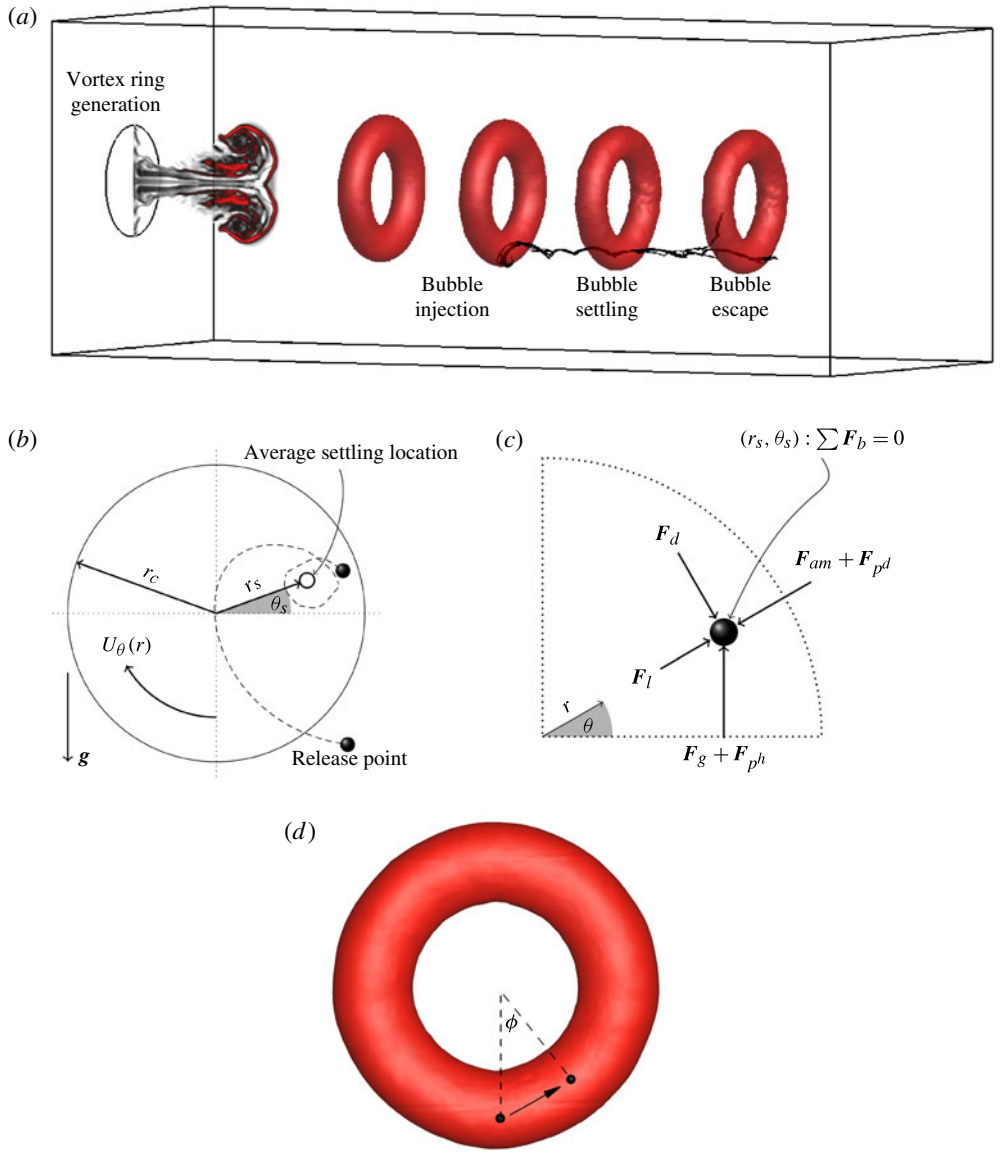

FIGURE 3. (Colour online) Bubble entrainment and escape process in a travelling vortex ring created by an inlet pulse that rolls up and propagates downstream. (*a*) Bubble injection location and motion relative to the moving vortex core. (*b*) Settling location (r_s, θ_s) and a typical trajectory of bubbles in cylindrical coordinates. (*c*) Mean force balance occurring at the settled location (here $\boldsymbol{F}_d$ is drag, $\boldsymbol{F}_\ell$ is lift, $\boldsymbol{F}_{am}$ is added mass, $\boldsymbol{F}_g$ is gravity and $\boldsymbol{F}_p$ is the pressure force, with sub-indices h and d representing the hydrostatic and dynamic components, respectively). (*d*) Bubble escape path along the centre of the vortex core, measured as an angle ϕ on either side of the plane of bubble injection.

balance of the pressure ($\boldsymbol{F}_p$), added mass ($\boldsymbol{F}_{am}$), lift ($\boldsymbol{F}_\ell$), drag ($\boldsymbol{F}_d$) and gravity forces ($\boldsymbol{F}_g$), respectively (Sridhar & Katz 1999; Finn *et al.* 2011; Rastello *et al.* 2011). For the cases studied in the present work, the angle (θ_s) at which the bubbles settle is

typically small ($\theta_s \to 0$) and, under such a situation, the gravity and buoyancy forces are approximately balanced by the drag force, whereas the radial settling location (r_s) is then obtained from an approximate balance of the lift, the added mass and the dynamic pressure-gradient forces, respectively. While the force balance broken up into these two components is only an approximation, it has been shown to be extremely accurate for these types of flows (Sridhar & Katz 1995; Finn *et al.* 2011). As the bubbles entrain and settle, their presence forces an alteration of the local flow field, which can result in observable levels of distortion. If this distortion becomes significant, the bubbles tend to leave the plane of injection and escape laterally along the vortex core centre; see figure 3(*d*). Once the bubbles escape the plane of injection, the vortex ring along this plane can slowly begin to repair itself back to a structure similar to its pre-bubble entrainment form in some cases. Using this system as a model problem, volume displacement effects will be shown to be significant even for very dilute volume loadings. These effects will be measured and their influence on the carrier phase analysed.

The rest of the paper is arranged as follows. In § 2 we will present the mathematical formulation, a brief description of the numerical method, and an analysis technique for volume displacement effects, specifically how they can be isolated and measured. The simulation set-up is described in § 3.1. Section 3.2 discusses the behaviour of both phases, showing agreement with experimental data. Quantification of vortex distortion, bubble escape and their effects on the forces on the bubbles are presented in § 3.3. The vortex distortion effects are explained by qualitatively correlating them to the wake structures created by the bubbles in § 3.4. In § 4 we quantify and analyse these volumetric coupling effects in our system and propose a simplified model to improve the two-way coupling momentum transfer approach in a consistent manner. A summary of the results and some conclusions are given in § 5.

2. Mathematical formulation

In the present volumetric coupling formulation, the bubbles are assumed spherical, subgrid scale and constant in size. Standard Lagrangian particle tracking is performed to track the centroid of the bubble by using closure models for the various forces exerted by the flow on the bubbles. The reaction from the bubbles to the fluid is handled as a point source, similar to the two-way coupling methodology. In addition, the effect of fluid displaced by the bubbles is accounted for through the local bubble volume fractions, computed by mapping the Lagrangian bubble location and its volume onto a fixed Eulerian grid used for fluid flow solutions. In the present work, all scales associated with the undisturbed fluid flow are captured on the computational grid by using a fine enough mesh, similar to a direct numerical solution procedure. Bubble–bubble collisions are neglected because only eight bubbles ($300\ \mu\text{m} < d_b < 1300\ \mu\text{m}$) are used in all the cases studied, resulting in extremely low volume fractions ($10^{-5} < VF < 10^{-3}$; see figure 2). The volume fraction is based on the slice of the bottom of the vortex ring around which the bubbles settle, not the entire domain. It was also verified in the computation that the bubble trajectories do not frequently cross over the duration of the simulation.

2.1. *Dispersed phase*

The bubble phase is handled using the equations of motion developed by Gatignol (1983) and Maxey (1983). Forces on bubbles are computed from explicit carrier (liquid) phase information. The forces are used to update the bubble velocity and

position by solving the following system of ordinary differential equations:

$$\frac{\mathrm{d}}{\mathrm{d}t}(\boldsymbol{x}_b) = \boldsymbol{u}_b, \tag{2.1}$$

$$m_b \frac{\mathrm{d}}{\mathrm{d}t}(\boldsymbol{u}_b) = \sum \boldsymbol{F}_b. \tag{2.2}$$

Here, $\boldsymbol{x}_b$ is the bubble location, m_b is the mass of an individual bubble, $\boldsymbol{u}_b$ is the bubble velocity vector and $\boldsymbol{F}_b$ denotes the force acting on a bubble. In this case $\boldsymbol{F}_b$ can be broken up into the gravity ($\boldsymbol{F}_g$), drag ($\boldsymbol{F}_d$), lift ($\boldsymbol{F}_\ell$), added mass ($\boldsymbol{F}_{am}$) and pressure ($\boldsymbol{F}_p$) forces on the bubble:

$$\sum \boldsymbol{F}_b = \boldsymbol{F}_g + \boldsymbol{F}_d + \boldsymbol{F}_\ell + \boldsymbol{F}_{am} + \boldsymbol{F}_p. \tag{2.3}$$

The gravitational force is simply taken as the weight of the bubble, where $\boldsymbol{g}$ is the gravitational acceleration ($\boldsymbol{g} = 9.81$ m s^{-2} vertically), and is given as

$$\boldsymbol{F}_g = -\rho_b \mathscr{V}_b \boldsymbol{g}, \tag{2.4}$$

where the volume of the individual particle is denoted by $\mathscr{V}_b$ and the bubble density is ρ_b.

The drag force on the bubble is modelled using the standard drag equation for flow past a sphere,

$$\boldsymbol{F}_d = -\tfrac{1}{8} C_d \rho_\ell \pi d_b^2 |\boldsymbol{u}_b - \boldsymbol{u}_{\ell,b}|(\boldsymbol{u}_b - \boldsymbol{u}_{\ell,b}), \tag{2.5}$$

where C_d is the drag coefficient, ρ_ℓ is the liquid density, d_b is the bubble diameter, $\boldsymbol{u}_b$ is the bubble velocity and $\boldsymbol{u}_{\ell,b}$ is the local fluid velocity vector interpolated at the bubble centroid. This solid-sphere drag model choice is appropriate for this system because the impurities that gather on the bubble surface create a no-slip condition (Harper 1972; Magnaudet & Eames 2000). Experiments (Sridhar & Katz 1995) also indicate the presence of 'dirty' bubbles. This choice of a drag model has been verified in the experimental work of Sridhar & Katz (1995), and is consistent with the lift model given here. Here, $\boldsymbol{u}_{\ell,b}$ strictly denotes the 'undisturbed' fluid velocity at the bubble location, which is close to the local fluid velocity for small, subgrid bubbles, as studied in this work. For larger bubbles, finding $\boldsymbol{u}_{\ell,b}$ is not straightforward, and may require additional modelling, including stochastic components to the drag forces. Such second-order changes to the drag force may alter the bubble trajectory slightly, but its influence on the volume displacement effects to be studied in this work is negligible. For the Reynolds-number ranges and bubble mass loadings being studied here, the Schiller & Naumann (1935) drag curve has been selected. In this model, the drag coefficient is determined using

$$C_d = \frac{24}{Re_b}(1 + 0.15 Re_b^{0.687}), \tag{2.6}$$

in which Re_b is the bubble Reynolds number, given by $Re_b = (\rho_\ell d_b |\boldsymbol{u}_b - \boldsymbol{u}_{\ell,b}|)/\mu_\ell$, where μ_ℓ is the dynamic viscosity of the fluid. The bubble Reynolds numbers range over 20–160 for the cases studied in this work.

The lift force is modelled based on the experimentally determined lift model (Sridhar & Katz 1995) for this particular configuration,

$$\boldsymbol{F}_\ell = -C_\ell \rho_\ell \frac{\pi d_b^2}{4}(\boldsymbol{u}_b - \boldsymbol{u}_{\ell,b}) \times (\boldsymbol{\nabla} \times \boldsymbol{u}_{\ell,b}). \tag{2.7}$$

In the present work, the lift coefficient is based on the experimentally determined model (Sridhar & Katz 1995) and is given as

$$C_\ell = 0.22\alpha^{-3/4} \quad \text{where } \alpha = \frac{|\nabla \times \boldsymbol{u}_{\ell,b}|d_b}{2|\boldsymbol{u}_{\ell,b} - \boldsymbol{u}_b|}. \tag{2.8}$$

In their experimental study, Sridhar & Katz (1995) emphasized the importance of C_ℓ on bubble trajectory and settling location. Their experimentally determined lift model gave higher coefficients, C_ℓ, than most analytically developed models. The higher lift coefficients are due to contaminants on the bubble–liquid interface causing a change from a no-shear condition to a no-slip condition at the interface. This yields high bubble spin rates and thus the higher lift coefficients (Sridhar & Katz 1995; Rastello *et al.* 2009).

The added mass force ($\boldsymbol{F}_{am}$) is modelled as

$$\boldsymbol{F}_{am} = -\frac{1}{2}\rho_\ell \mathscr{V}_b \left(\frac{\mathrm{d}\boldsymbol{u}_b}{\mathrm{d}t} - \frac{\mathrm{D}\boldsymbol{u}_{\ell,b}}{\mathrm{D}t} \right). \tag{2.9}$$

Here, $\mathrm{D}/\mathrm{D}t$ is the total derivative following a fluid parcel and $\mathrm{d}/\mathrm{d}t$ is the derivative following the bubble velocity. The standard added mass coefficient of $1/2$ is used.

The far-field pressure force on the bubbles is due to the buoyancy force (hydrostatic pressure gradient), the inertial forces and the viscous strains,

$$\boldsymbol{F}_p = -\mathscr{V}_b \nabla p. \tag{2.10}$$

A short note on the history force is given here. The history force can be modelled as

$$\boldsymbol{F}_h = \frac{3\pi d_b^2 \mu_\ell}{2} \int_0^t \frac{\mathrm{d}(\boldsymbol{u}_b - \boldsymbol{u}_{\ell,b})/\mathrm{d}\tau}{\sqrt{\pi \nu_\ell (t-\tau)}}\, \mathrm{d}\tau. \tag{2.11}$$

The history force effects were shown to be smaller than 6 % of the buoyancy force at any time for this system (Sridhar & Katz 1995). Owing to the settling nature of the bubbles in this system, once the bubbles are settled, the history effect is small, as the relative acceleration is not large compared to $\|\boldsymbol{u}_{\ell,b} - \boldsymbol{u}_b\|^2 / d_b$ (Merle, Legendre & Magnaudet 2005). The history force is neglected in this work, as its maximum magnitude was determined to be less than one-third of the smallest force component on the bubbles at any time.

2.2. *Continuous phase*

In the volumetric coupling formulation, the fluid-phase equations are altered to account for the mass displaced by the presence and motion of the bubbles (Joseph *et al.* 1990). Each bubble occupies a volume, $\mathscr{V}_b$, which corresponds to a local bubble volume fraction, θ_b. The local liquid volume fraction is defined as $\theta_\ell = 1 - \theta_b$. Accounting for the mass of the bubble within a control volume, the conservation of mass becomes

$$\frac{\partial}{\partial t}(\rho_\ell \theta_\ell) + \nabla \cdot (\rho_\ell \theta_\ell \boldsymbol{u}_\ell) = 0, \tag{2.12}$$

where ρ_ℓ is the liquid density. No summation is implied on the subscript ℓ. Note that in this form the flow field, even for an incompressible fluid, is not divergence-free as long as the volume fraction changes with time or has spatial gradients. Rearrangement of (2.12) yields an expression for the local divergence,

$$\nabla \cdot \boldsymbol{u}_\ell = -\frac{1}{\theta_\ell}\left(\frac{\partial \theta_\ell}{\partial t} + \boldsymbol{u}_\ell \cdot \nabla \theta_\ell \right) = -\frac{1}{\theta_\ell}\frac{\mathrm{D}\theta_\ell}{\mathrm{D}t}. \tag{2.13}$$

In a similar manner, the conservation-of-momentum equation is altered to include the presence of bubbles (Joseph *et al.* 1990; Gidaspow 1994; Jackson 1997; Zhang & Prosperetti 1997),

$$\frac{\partial}{\partial t}(\rho_\ell \theta_\ell \boldsymbol{u}_\ell) + \boldsymbol{\nabla}\cdot(\rho_\ell \theta_\ell \boldsymbol{u}_\ell \boldsymbol{u}_\ell) = -\boldsymbol{\nabla} p + \boldsymbol{\nabla}\cdot(\mu_\ell \theta_\ell \boldsymbol{D}) - \theta_\ell \rho_\ell \boldsymbol{g} + \boldsymbol{f}^t_{b\to\ell}, \tag{2.14}$$

where p is the dynamic pressure in the fluid phase, and $\boldsymbol{D} = \boldsymbol{\nabla}\boldsymbol{u}_\ell + \boldsymbol{\nabla}\boldsymbol{u}_\ell^T$ is the deformation tensor. The total reaction force ($\boldsymbol{f}^t_{b\to\ell}$) from the bubbles onto the fluid per unit mass of fluid contains contributions from the surface forces and is given as

$$\boldsymbol{f}^t_{b\to\ell}(\boldsymbol{x}_{cv}) = -\sum_{b=1}^{N_b} \mathscr{G}_\Delta(\boldsymbol{x}_{cv}, \boldsymbol{x}_b)(\boldsymbol{F}_p + \boldsymbol{F}_d + \boldsymbol{F}_\ell + \boldsymbol{F}_{am}), \tag{2.15}$$

where $\mathscr{G}_\Delta$ denotes the interpolation function from the bubble locations on to the Eulerian grid and is constrained by the conservation condition $\int_{\mathscr{V}} \mathscr{G}_\Delta \,\mathrm{d}\mathscr{V} = 1$. In the present work, a Gaussian interpolation function is used; see Apte *et al.* (2008) and Shams *et al.* (2011) for details. Here $\boldsymbol{x}_{cv}$ and $\boldsymbol{x}_b$ are the centres of the control volume and bubble, respectively, and N_b is the total number of bubbles in the neighbourhood of the control volume centred at $\boldsymbol{x}_{cv}$.

Note that the total force on the bubble consists of the pressure force, $F_p = -\mathscr{V}_b \boldsymbol{\nabla} p$. The reaction of this force onto the fluid phase results in the force density $+\theta_b \boldsymbol{\nabla} p$. The governing equation then becomes

$$\begin{aligned}\frac{\partial}{\partial t}(\rho_\ell \theta_\ell \boldsymbol{u}_\ell) + \boldsymbol{\nabla}\cdot(\rho_\ell \theta_\ell \boldsymbol{u}_\ell \boldsymbol{u}_\ell) \\ = -\boldsymbol{\nabla} p + \boldsymbol{\nabla}\cdot(\theta_\ell \mu_\ell \boldsymbol{D}) - \theta_\ell \rho_\ell \boldsymbol{g} + \boldsymbol{f}_{b\to\ell} + \underbrace{\theta_b \boldsymbol{\nabla} p}_{\boldsymbol{F}_p \text{ force density}},\end{aligned} \tag{2.16}$$

where $\theta_b \boldsymbol{\nabla} p$ is the Eulerian force density obtained from the pressure force and $\boldsymbol{f}_{b\to\ell}$ is the Eulerian force density constructed from the Lagrangian force on the bubbles without the pressure force (equation (2.15) without the pressure force, $\boldsymbol{F}_p$). Noting that $\theta_b + \theta_\ell = 1$, the above equation (2.16) can be rewritten in a more commonly used form by combining the first and last terms on the right-hand side:

$$\frac{\partial}{\partial t}(\rho_\ell \theta_\ell \boldsymbol{u}_\ell) + \boldsymbol{\nabla}\cdot(\rho_\ell \theta_\ell \boldsymbol{u}_\ell \boldsymbol{u}_\ell) = -\theta_\ell \boldsymbol{\nabla} p + \boldsymbol{\nabla}\cdot(\theta_\ell \mu_\ell \boldsymbol{D}) - \theta_\ell \rho_\ell \boldsymbol{g} + \boldsymbol{f}_{b\to\ell}. \tag{2.17}$$

This formulation is commonly used in gas-fluidized beds (Kuipers *et al.* 1993; Gidaspow 1994; Darmana, Deen & Kuipers 2006; van der Hoef *et al.* 2008). Note that, in the absence of any fluid velocity, but in the presence of bubbles, the pressure-gradient force is then appropriately balanced by the gravity force. The pressure-gradient and the gravitational terms can also be combined together to remove the hydrostatic part of the pressure field by dropping the gravitational term in the momentum equation. In such a case, the gravitational force on the bubble (equation (2.4)) typically includes the buoyancy force.

The only difference between the volumetric and two-way coupling approach is that in the two-way coupling model it is assumed that the volume occupied by the bubbles is negligibly small. That is, in the two-way coupling model, for a control volume containing bubbles, the liquid volume fraction θ_ℓ is still assumed to be equal to 1. The two-way coupling formulation can be obtained by simply setting $\theta_\ell = 1$ in all terms of the continuity and momentum equations (2.12) and (2.14) or (2.17). For completeness,

the standard point-particle two-way coupling continuity and momentum equations are

$$\boldsymbol{\nabla} \cdot \boldsymbol{u}_\ell = 0, \tag{2.18}$$

$$\rho_\ell \left(\frac{\partial \boldsymbol{u}_\ell}{\partial t} + \boldsymbol{\nabla} \cdot (\boldsymbol{u}_\ell \boldsymbol{u}_\ell) \right) = -\boldsymbol{\nabla} p + \mu_\ell (\boldsymbol{\nabla} \cdot \boldsymbol{D}) - \rho_\ell \boldsymbol{g} + \boldsymbol{f}_{b\to\ell}. \tag{2.19}$$

2.3. *Numerical method*

Details of the mathematical formulation and numerical method can be found in Finn *et al.* (2011) and Shams *et al.* (2011), so only a brief description is given here. The above set of variable density equations (owing to local variations in fluid volume fractions) are solved using a pressure-based, second-order, fractional time-stepping scheme on a collocated grid arrangement. The velocity, pressure and volume fractions are stored at the centroids of the volumes. The Lagrangian bubble equations are advanced first using a simple forward Euler approximation with subcycling within each fluid time step (Shams *et al.* 2011) to accurately account for the bubble time scales relative to the flow time scales. Knowing the bubble locations, the bubble and fluid volume fractions are computed at cell centres. The cell-centred velocities (or $\rho_\ell \theta_\ell \boldsymbol{u}_\ell$) are advanced by solving the momentum equation as a predictor step. The predicted velocities are interpolated to the faces and then projected to satisfy the continuity constraint. Projection yields the pressure potential at the cell centres, and its gradient is used to correct the cell and face-normal velocities. With the volumetric coupling formulation, the pressure term in the momentum equation (2.17) is multiplied by the local fluid volume fraction (θ_ℓ), and a standard projection operation yields a variable-coefficient Poisson equation. Shams *et al.* (2011) have shown how to preserve the constant-coefficient pressure Poisson equation, by treating part of the pressure-gradient term in the momentum equation as a subgrid, Lagrangian reaction source term, and accelerating the solution procedure with use of algebraic multigrid techniques. The solver is fully parallel and has been verified for a variety of particle-laden flows (Apte *et al.* 2008; Shams & Apte 2010; Finn *et al.* 2011).

The details of the simulation set-up are given in § 3.1.

2.4. *Measuring volumetric influences*

The volume displacement effects in the volumetric coupling formulation play an integral role in properly modelling the equations for conservation of mass and momentum. It is important to understand how these effects manifest themselves, and a method of quantification in comparison with the standard two-way coupling point-source approach is needed. In order to find the magnitude of the volume displacement forces on the flow, an expression for the source term due to volume displacement effects is derived by writing the original conservative form of the governing equations in a non-conservative form and expressing the additional terms in comparison with the two-way coupling formulation as the *volume displacement force*. Equation (2.20) gives the volumetric coupling momentum equations in the conservative form, with $\boldsymbol{f}_{b\to\ell}$ being the two-way coupling source term:

$$\begin{aligned} &\frac{\partial (\rho_\ell \theta_\ell \boldsymbol{u}_\ell)}{\partial t} + \boldsymbol{\nabla} \cdot (\rho_\ell \theta_\ell \boldsymbol{u}_\ell \boldsymbol{u}_\ell) \\ &\quad = -\theta_\ell \boldsymbol{\nabla} p + \boldsymbol{\nabla} \cdot [\mu_\ell \theta_\ell (\boldsymbol{\nabla} \boldsymbol{u}_\ell + \boldsymbol{\nabla} \boldsymbol{u}_\ell^T)] + \boldsymbol{f}_{b\to\ell} - \rho_\ell \theta_\ell \boldsymbol{g}. \end{aligned} \tag{2.20}$$

The first two terms are then expanded in a non-conservative form to obtain

$$\underbrace{\boldsymbol{u}_\ell\left(\frac{\partial(\rho_\ell\theta_\ell)}{\partial t}+\boldsymbol{\nabla}\cdot(\rho_\ell\theta_\ell\boldsymbol{u}_\ell)\right)}_{(I)}+\rho_\ell\theta_\ell\left(\frac{\partial\boldsymbol{u}_\ell}{\partial t}+\boldsymbol{u}_\ell\cdot\boldsymbol{\nabla}\boldsymbol{u}_\ell\right)$$
$$=-\theta_\ell\boldsymbol{\nabla}p+\boldsymbol{\nabla}\cdot(\mu_\ell\theta_\ell(\boldsymbol{\nabla}\boldsymbol{u}_\ell+\boldsymbol{\nabla}\boldsymbol{u}_\ell^T))+\boldsymbol{f}_{b\to\ell}-\rho_\ell\theta_\ell\boldsymbol{g}. \tag{2.21}$$

Utilizing conservation of mass, term (I) vanishes, and it gives

$$\rho_\ell\theta_\ell\left(\frac{\partial\boldsymbol{u}_\ell}{\partial t}+\boldsymbol{u}_\ell\cdot\boldsymbol{\nabla}\boldsymbol{u}_\ell\right)=-\theta_\ell\boldsymbol{\nabla}p+\boldsymbol{\nabla}\cdot[\mu_\ell\theta_\ell(\boldsymbol{\nabla}\boldsymbol{u}_\ell+\boldsymbol{\nabla}\boldsymbol{u}_\ell^T)]+\boldsymbol{f}_{b\to\ell}-\rho_\ell\theta_\ell\boldsymbol{g}. \tag{2.22}$$

The above equation can be rewritten using the product rule for the advective terms and rearranging to get

$$\rho_\ell\theta_\ell\left(\frac{\partial\boldsymbol{u}_\ell}{\partial t}+\boldsymbol{\nabla}\cdot(\boldsymbol{u}_\ell\boldsymbol{u}_\ell)\right)$$
$$=-\theta_\ell\boldsymbol{\nabla}p+\boldsymbol{\nabla}\cdot[\mu_\ell\theta_\ell(\boldsymbol{\nabla}\boldsymbol{u}_\ell+\boldsymbol{\nabla}\boldsymbol{u}_\ell^T)]+\boldsymbol{f}_{b\to\ell}-\rho_\ell\theta_\ell\boldsymbol{g}+\rho_\ell\theta_\ell(\boldsymbol{u}_\ell\boldsymbol{\nabla}\cdot\boldsymbol{u}_\ell). \tag{2.23}$$

To find the forcing terms arising from the volume displacement effect, (2.23) is compared to the traditional one-way coupling equations for an incompressible fluid with an additional source $\widehat{\Delta\boldsymbol{V}}$ given as

$$\rho_\ell\left(\frac{\partial\boldsymbol{u}_\ell}{\partial t}+\boldsymbol{\nabla}\cdot(\boldsymbol{u}_\ell\boldsymbol{u}_\ell)\right)=-\boldsymbol{\nabla}p+\boldsymbol{\nabla}\cdot[\mu_\ell(\boldsymbol{\nabla}\boldsymbol{u}_\ell+\boldsymbol{\nabla}\boldsymbol{u}_\ell^T)]-\rho_\ell\boldsymbol{g}+\widehat{\Delta\boldsymbol{V}}. \tag{2.24}$$

Note that the advective terms in (2.24) (and hence in (2.23) as well) are written in a conservative form, mainly because, for incompressible flows, the numerical approach uses this form for discrete approximations. The source $\widehat{\Delta\boldsymbol{V}}$ can be obtained by subtracting (2.24) from (2.23):

$$\widehat{\Delta\boldsymbol{V}}=\underbrace{\theta_b\boldsymbol{\nabla}p}_{(\widehat{\Delta\boldsymbol{V}}_1)}+\underbrace{\rho_\ell\theta_b\left(\frac{\partial\boldsymbol{u}_\ell}{\partial t}+\boldsymbol{\nabla}\cdot(\boldsymbol{u}_\ell\boldsymbol{u}_\ell)\right)}_{(\widehat{\Delta\boldsymbol{V}}_2)}-\underbrace{\mu_\ell[\boldsymbol{\nabla}\cdot\theta_b(\boldsymbol{\nabla}\boldsymbol{u}_\ell+\boldsymbol{\nabla}\boldsymbol{u}_\ell^T)]}_{(\widehat{\Delta\boldsymbol{V}}_3)}$$
$$+\underbrace{\boldsymbol{f}_{b\to\ell}}_{(\widehat{\Delta\boldsymbol{V}}_4)}+\underbrace{\rho_\ell\theta_b\boldsymbol{g}}_{(\widehat{\Delta\boldsymbol{V}}_5)}+\underbrace{\rho_\ell\theta_\ell\boldsymbol{u}_\ell(\boldsymbol{\nabla}\cdot\boldsymbol{u}_\ell)}_{(\widehat{\Delta\boldsymbol{V}}_6)}. \tag{2.25}$$

The net source includes both the liquid displacement effects, due to spatial and temporal volume fraction gradients, as well as the two-way momentum coupling force.

The terms on the right-hand side of (2.25) can be interpreted as follows:

$$\widehat{\Delta\boldsymbol{V}}_1=\text{local pressure-gradient term,} \tag{2.26a}$$
$$\widehat{\Delta\boldsymbol{V}}_2=\text{unsteady and fluid inertial terms,} \tag{2.26b}$$
$$\widehat{\Delta\boldsymbol{V}}_3=\text{viscous stresses due to volume fraction variation,} \tag{2.26c}$$
$$\widehat{\Delta\boldsymbol{V}}_4=\text{point-source momentum transfer term,} \tag{2.26d}$$
$$\widehat{\Delta\boldsymbol{V}}_5=\text{hydrostatic buoyancy term,} \tag{2.26e}$$
$$\widehat{\Delta\boldsymbol{V}}_6=\text{local flow divergence term.} \tag{2.26f}$$

Note that $\widehat{\Delta \boldsymbol{V}}_1$ and $\widehat{\Delta \boldsymbol{V}}_4$ can be combined together to obtain the net two-way coupling momentum source $\boldsymbol{f}^t_{b\to\ell}$. By separating out volume displacement effects in this manner, it is possible to measure the relative influence of these effects compared to the traditional two-way coupling momentum transfer formulation given by (2.18) and (2.19).

3. Results

3.1. *Simulation set-up*

The vortex ring is generated within a rectangular box of dimensions 0.8 m × 0.3 m × 0.3 m in the streamwise ($\hat{x}$), vertical ($\hat{y}$) and lateral ($\hat{z}$) directions, respectively. This domain size was found to be sufficient based on previous two-dimensional studies (Finn *et al.* 2011) and provides appropriate amount of field of view for bubbles to get entrained within the ring and influence the ring after settling. In addition, it was verified that further increase in the domain size does not alter the vortex-ring structure or its propagation.

The inlet pipe section is of radius 0.05 m and centred around the $x = 0$ plane, the inlet injects a pulse of fluid generating the vortex ring, which is captured by using a simple Cartesian grid. This was found to give clean generation of the vortex ring as opposed to use of tetrahedral unstructured grids. A Cartesian grid, 800 × 241 × 241, is utilized in this work. Cell spacing is coarse in the corners and dense in the centre to resolve the inlet section as well as the region of interest accurately. For studying vortex-ring formation, Mohseni, Ran & Colonius (2001) used a grid resolution of 1/25th of the inlet radius to achieve grid convergence. The finest grid used in this study has even finer spacing of 1/50th of the inlet radius in order to resolve the inlet ring generation accurately. Several grid resolutions were studied to ensure proper vortex behaviour. This was monitored by computing the vortex-ring evolution and its strength decay from the inlet to the exit. With the fine grid resolution used in this study, the vortex ring propagates for the length of the numerical experiment with minimal dissipation of the vortex strength, in line with experimental observations. The time step was kept constant at $\Delta t = 0.001$ s in order to accurately capture the temporal evolution of the vortex-ring and bubble dynamics. The inlet velocity profile (see figure 4) is assigned through a polynomial interpolation of the experimental profile; see Finn *et al.* (2011) for details. The inlet condition is handled as a velocity source, which accurately represents the experimental piston inlet profile of the experiments (James & Madnia 1996). In order to achieve the three different strengths of vortex rings studied in this work, the cylindrical slug model of Glezer (1988) is used to match the experimental data. The vortex strength, Γ_0, is computed as shown in (3.1), with its associated vortex Reynolds number (Re_{vx}) in (3.2):

$$\Gamma_0 = \int_0^T \frac{u_0^2(t)}{2}\,\mathrm{d}t = 0.0159,\ 0.0207,\ 0.0254\ \mathrm{m^2\ s^{-1}}, \tag{3.1}$$

$$Re_{vx} = \frac{1}{2\nu_\ell}\int_0^T u_0^2(t)\,\mathrm{d}t = 15\,900,\ 20\,700,\ 25\,400. \tag{3.2}$$

The inlet velocity profile is scaled by a constant value for the three different vortex strengths. The weakest of the three strengths, $\Gamma_0 = 0.0159\ \mathrm{m^2\ s^{-1}}$, constitutes a transitional vortex, while the two stronger vortices can be classified as turbulent based on Glezer (1988). As the liquid enters into the ambient domain, a shear layer forms that rolls up to create a vortex ring that strengthens as the inlet pulse

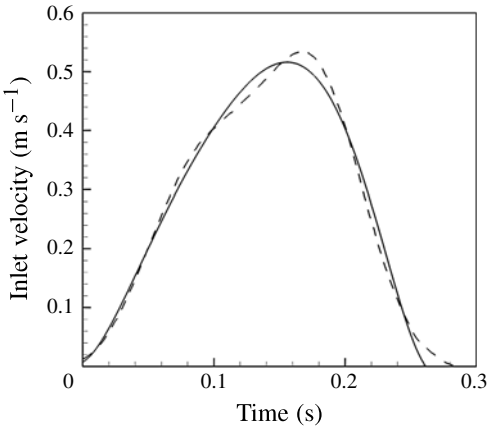

FIGURE 4. Inlet velocity profile used for generating the vortex ring: present work (—) and experimental data of Sridhar & Katz (1999) (- - -).

Case no.	Γ_0 (m^2 s^{-1})	$2r_b$ (μm)	St_b	$gr_b^3/\Gamma_0^2(\times10^6)$	r_b/r_c	$2r_b/\Delta_{cv}$	$VF(\times10^4)$
1	0.0159	300	0.09	0.13	0.013	0.21	0.11
2	0.0159	500	0.27	0.61	0.022	0.35	0.51
3	0.0159	700	0.53	1.66	0.031	0.50	1.39
4	0.0159	900	0.87	3.54	0.039	0.65	2.96
5	0.0159	1100	1.30	6.46	0.048	0.79	5.42
6	0.0159	1300	1.81	10.66	0.057	0.93	8.94
7	0.0207	700	0.68	0.98	0.031	0.50	1.39
8	0.0254	500	0.43	0.24	0.022	0.35	0.51
9	0.0254	700	0.84	0.60	0.031	0.50	1.39
10	0.0254	900	1.39	1.39	0.039	0.65	2.96
11	0.0254	1100	2.07	2.53	0.048	0.79	5.42
12	0.0254	1300	2.89	4.18	0.057	0.93	8.94

TABLE 1. Parameter variations for travelling vortex-ring cases. Here Γ_0 is the vortex strength, r_b is bubble radius, r_c is vortex core radius, St_b is the bubble Stokes number, Δ_{cv} is the local grid resolution and VF is the volume loading.

dissipates. The generated travelling vortex ring propagates to the end of the domain. The ring maintains a consistent structure during the entire path of its motion. The core propagation speeds, averaged over the entire time of the simulation, are 0.11, 0.16 and 0.19 m s^{-1} for the three strengths, respectively. The vortex ring formed from this process is symmetric, as plotted in figure 3(*a*) based on the computed flow.

Table 1 lists the various cases studied in this work, similar to those studied in Sridhar & Katz (1999) and Finn *et al.* (2011). Three different vortex strengths, weak ($\Gamma_0 = 0.0159$ m^2 s^{-1}), medium (0.0207 m^2 s^{-1}) and strong (0.0254 m^2 s^{-1}), are used for generating the travelling vortex ring. A wide range of bubble diameters (300–1300 μm) are injected to study their effect on the vortex. For the cases studied, the ratio of bubble diameter to grid resolution, d_b/Δ_{cv}, is less than one and ranges between 0.21 and 0.93. The volume loading of the disperse phase is based on only the

region of the vortex core where bubbles are present, not on the entire domain, but is still very small.

Let the vortex core radius, r_c, be the length scale, the velocity at the settling location, $U_{rel} = \Gamma_0 r_s/2\pi r_c^2$, be the velocity scale, and $\rho_\ell r_s \Gamma_0^2/4\pi^2 r_c^4$ be the local pressure-gradient scale at the bubble settling location for the flow structure in a vortex ring. Then, the following non-dimensional groups can be obtained for the bubble dynamics and bubble settling location (Sridhar & Katz 1999):

$$\bar{r}_s = r_s/r_c, \quad \bar{r}_b = r_b/r_c, \quad \bar{g} = g r_c^3/\Gamma_0^2 \quad \text{and} \quad Re_{vx} = \Gamma_0/\nu_\ell, \tag{3.3}$$

where $\bar{r}_s$ is the non-dimensional settling location, $\bar{r}_b$ is the non-dimensional bubble radius, $\bar{g}$ is the non-dimensional gravity force and Re_{vx} is the vortex Reynolds number. The non-dimensional gravity force is proportional to the ratio of the weight of the fluid in the vortex core to the integrated pressure gradient in the core. In the present cases, the vortex core size (r_c) remains roughly constant for all cases and is much larger than the bubble size (r_b). Then $\bar{r}_b$ and $\bar{g}$ can be combined to form a non-dimensional group ($g r_b^3/\Gamma_0^2$), which becomes the ratio of the buoyancy force on the bubble to the hydrodynamic pressure-gradient force. The non-dimensional settling location ($\bar{r}_s$) is then a function of this parameter ($\bar{g}\bar{r}_b^3$) and the vortex Reynolds number. The Reynolds number dependence mainly comes through the drag and lift coefficients, which can depend on the bubble size and bubble (or vortex) Reynolds number.

Likewise, $\bar{r}_b$ and Re_{vx} can be combined to obtain the bubble Stokes number,

$$St_b = (\overline{\omega})\left(\frac{\rho_b d_b^2}{36\mu_\ell}\right) = \left(\frac{\Gamma_0}{\pi r_c^2}\right)\left(\frac{\rho_b d_b^2}{36\mu_\ell}\right) = \frac{1}{9\pi}\frac{\rho_b}{\rho_\ell}\bar{r}_b^2 Re_{vx} = \frac{1}{9}\frac{\rho_b}{\rho_\ell}\frac{\bar{r}_b}{\bar{r}_s}Re_b^{ref}, \tag{3.4}$$

where $Re_b^{ref} = U_{rel} d_b/\nu_\ell$ is the reference bubble Reynolds number based on the bubble diameter. Bubble Stokes numbers range from 0.09 to 2.89, with three different vortex strengths. Sridhar & Katz (1999) argued that the bubble Reynolds number varies over a small range, $20 < Re_b^{ref} < 80$, for the given Stokes number range, whereas the gravity-based parameter ($\bar{g}\bar{r}_b^3$) varies by two orders of magnitude for the cases studied (see table 1) and assumed that the settling location is only a weak function of the Reynolds number.

3.2. *Bubble behaviour and vortex distortion*

The vortex ring is allowed to develop until it reaches 0.5 m downstream of the injection plane. The position of the vortex ring is tracked by finding the weighted centre of vorticity on the plane of bubble injection (the lowest two-dimensional slice of the core) with coordinates (X_c, Y_c), which are calculated as

$$X_c = \sum_i X_i \omega_i^2 \Big/ \sum_i \omega_i^2, \quad Y_c = \sum_i Y_i \omega_i^2 \Big/ \sum_i \omega_i^2. \tag{3.5}$$

In a perfectly symmetric vortex, the core centre would be at the point of zero velocity relative to the motion of the structure. In the bubble-free case, this is close but not exactly true, as the core has a slight asymmetry due to its travelling nature and turbulent features. In the bubble-laden cases, however, the two points of zero velocity and the weighted centre of vorticity may not be in close proximity owing to core fragmentation and asymmetry of the vortex core. When the vortex ring reaches 0.5 m, the bubbles are released in front of and below the core in the $z = 0$ plane containing part of the vortex ring, as shown in figure 3(*a*). Eight bubbles are injected individually

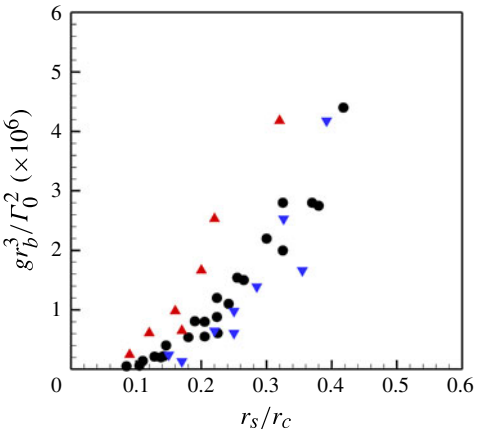

FIGURE 5. (Colour online) Ratio of buoyancy force to hydrodynamic pressure gradient versus the non-dimensional bubble settling location: two-way coupling (▲); volumetric coupling (▼); and experimental data of Sridhar & Katz (1999) (●).

every 10 ms. Each bubble is injected, then entrained separately. Although each bubble entrains at a different time, each follows a very similar path initially.

Figure 5 plots the gravity parameter (gr_b^3/Γ_0^2) versus the non-dimensional bubble settling locations ($\bar{r}_s = r_s/r_c$) for the cases studied, where $\bar{r}_s$ is the average position of the bubbles after entrainment into the first quadrant of the vortex. Predictions based on two-way and volumetric coupling formulations are compared with the experimental data of Sridhar & Katz (1999). It is observed that both formulations predict the basic trend that, as the ratio of the buoyancy to the pressure gradient is increased, the bubbles settle further away from the vortex centre. Similarly, for bubbles of the same size, increase in the vortex strength results in settling locations closer to the vortex core. The surface forces such as drag and lift are proportional to r_b^2, whereas the buoyancy, the added mass and pressure-gradient forces are proportional to r_b^3. The variability in the settling location with respect to the force ratio, gr_b^3/Γ_0^2, is attributed to the dimensional analysis process neglecting the dependence on the vortex Reynolds number. It is also observed that the two-way coupling formulation tends to underpredict the settling location for the entire range of ratios of buoyancy to hydrodynamic pressure gradient, with the error between the predicted location and the actual location being proportional to bubble size. The volumetric coupling formulation, however, provides better agreement with experimental results. It will be shown later that the fluid displacement effects present in the volumetric coupling formulation are critical in affecting the distribution of vorticity within the vortex core for bubbles that settle beyond $r_s/r_c > 0.2$, whereas the two-way coupling formulation showed a negligible effect on vorticity distribution (later in this section). It is also shown in § 4.4 that the fluid displacement effects, expressed as an equivalent momentum coupling force (2.25), show a dependence on the vortex Reynolds number (Γ_0/ν_ℓ).

Bubble trajectories relative to the vortex core centre are shown in figure 6 for the weak as well as the strong vortex cases with two representative bubble sizes. The coordinate system used to describe the bubble settling locations is shown in figure 3(*b*). The relative bubble positions are computed as $\boldsymbol{x}_{rel} = \boldsymbol{x}_b - \boldsymbol{X}_c$, then converted to cylindrical coordinates and plotted as (r_{rel}, θ_{rel}) on the plane of bubble injection, so $(0, 0)$ is the core centre as computed in (3.5). The differences in entrainment time

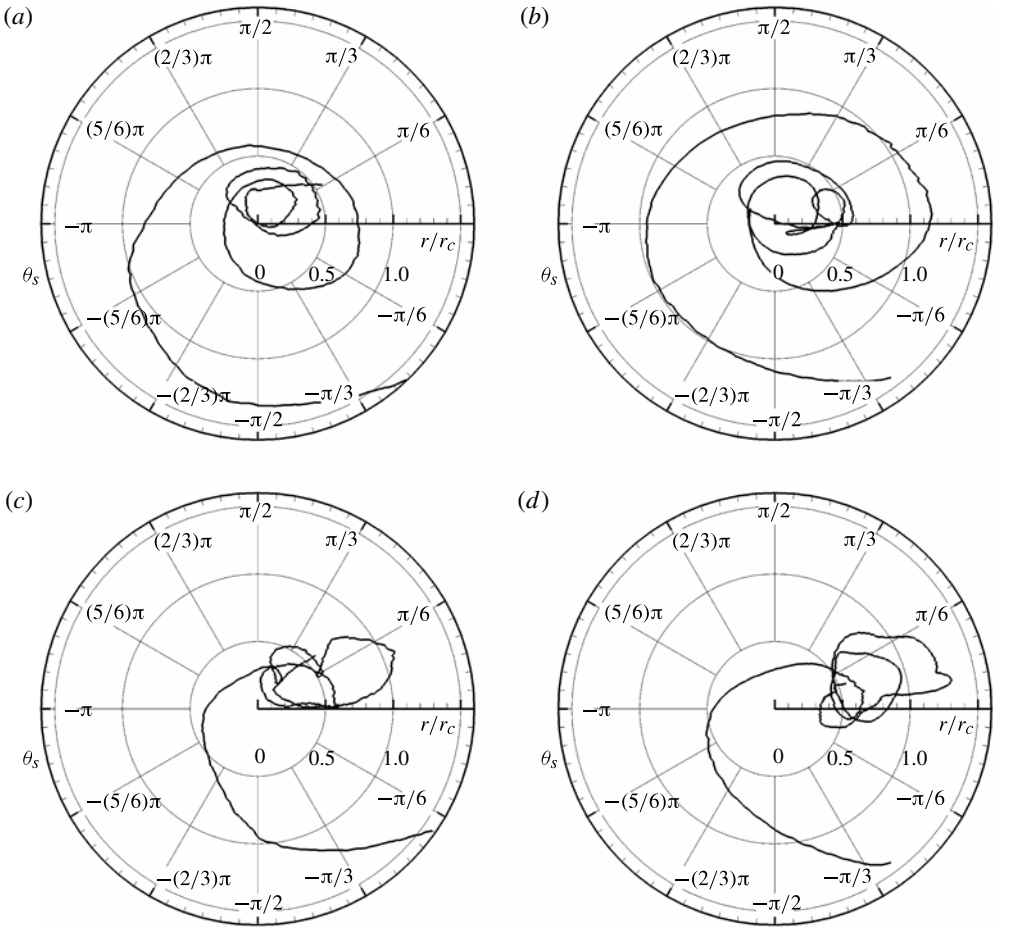

FIGURE 6. Bubble trajectories and settling locations relative to the vortex core centre: strong vortex cases (*a*) $d_b = 500$ μm (case no. 8) and (*c*) $d_b = 900$ μm (case no. 10); and weak vortex cases (*b*) 300 μm (case no. 1) and (*d*) 1100 μm (case no. 5).

and trajectories among the cases are easily noticeable. Large bubbles tend to take a more direct path to their settling location, whereas smaller bubbles take a longer route. For the present three-dimensional vortex-ring studies, the bubbles do not completely settle but tend to move in a small circular path around a mean settling location. Some of this may be due to the three-dimensional transitional flow within the vortex ring, since these were not observed in the two-dimensional work of Finn *et al.* (2011). These oscillations were, however, noted in experimental work, such as Rastello *et al.* (2009). For the weak vortex cases, large bubbles tend to show considerable volatility in settling position after they are entrained.

Compared to the past work on two-dimensional travelling vortex tubes (Finn *et al.* 2011), in the present three-dimensional simulations, the bubbles do not perfectly remain in the plane of injection for the entire duration of the simulation. After achieving a mean settling location in the plane of injection, the bubbles drifted from this plane as the vortex ring travelled downstream. This behaviour of the bubbles is referred to as *bubble escape* and is shown schematically in figure 3(*d*). Note that

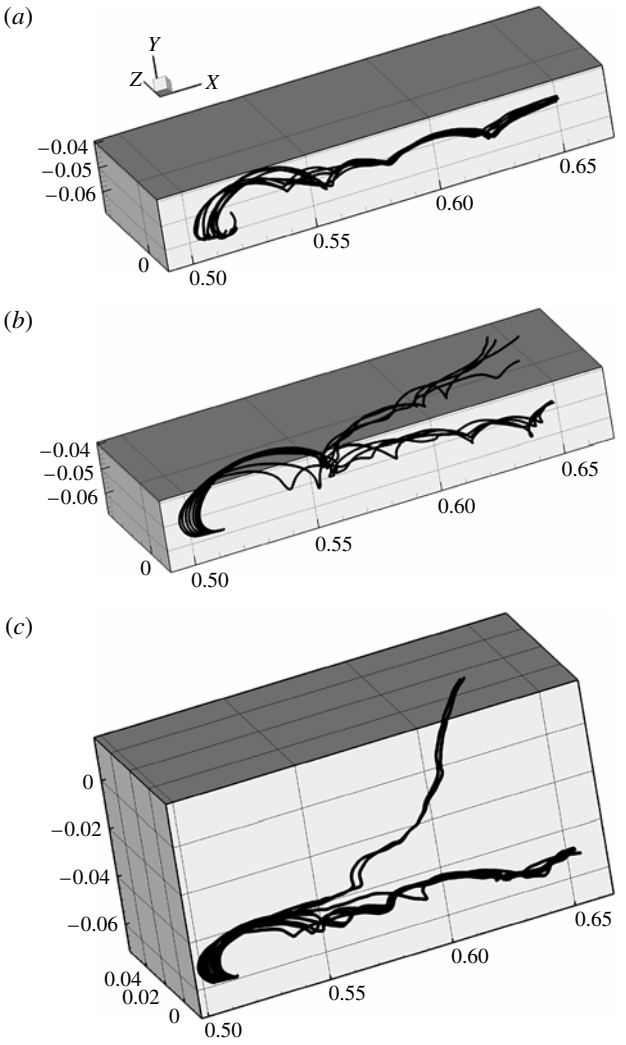

FIGURE 7. Paths traversed by bubbles within a vortex ring showing bubble escape: (*a*) marginal escape for strong vortex case no. 8 ($d_b = 500\ \mu$m); (*b*) moderate escape for weak vortex case no. 3 ($d_b = 700\ \mu$m); and (*c*) significant escape for weak vortex case no. 5 ($d_b = 1100\ \mu$m).

only minimal escape of the bubbles was obtained with two-way coupling computations, whereas significant escape is observed in some cases with volumetric coupling. In the vortex ring, bubbles escape to both sides of the plane of injection; however, for the sake of quantifying escape, the absolute value of the lateral ($\hat{z}$) component of their position is used in averaging their position along the core. This position is plotted at the end of simulation, i.e. when $X_c = 0.65$ m. It is observed that bubble escape is smaller for stronger vortex strength, whereas with weaker vortex ring the bubbles tend to escape more. The amount of bubble escape (i.e. angle ϕ from the plane of injection) changes with time. Figure 7 shows the escape trajectories of eight bubbles for representative strong and weak vortex strengths. For the strong vortex case (no. 8),

all eight bubbles stay relatively close together as they move downstream in the flow direction (x direction) and do not veer to either side of the vortex ring, showing minimal bubble escape. For the weak vortex case with 700 μm bubbles (case no. 3), the bubbles show moderate escape that increases as they travel downstream along with the vortex ring. Case no. 5 with large bubbles (1100 μm) shows significant escape, to an extent that the bubbles are no longer entrained into the vortex core at later times, but are still contained within the upper portions of the ring. As the bubbles escape from the injection plane, the vortex ring was found to begin to repair itself back to a structure similar to its pre-bubble entrainment form for some cases. This is found to be related to the variations in local bubble concentrations and hence the fluid displacement effects as discussed later.

Figure 8 shows the temporal evolution of the out-of-plane vorticity contours plotted in the moving cylindrical frame for unladen as well as bubble-laden cases for the weak vortex strength of $\Gamma_0 = 0.0159$ m^2 s^{-1}. The transitional nature of the vortex ring is evident. For the unladen case (as well as bubble-laden case computed using a two-way coupling reaction point source), a strong vortex core is observed (seen as the dark-grey (red online) spot at the centre) and remains mostly unaltered over the duration of the simulation. Figure 8 also shows the time evolution of the vortex ring when eight bubbles are entrained, obtained using the volumetric coupling formulation, in comparison with the corresponding unladen case. The four visualizations roughly correspond to positions of the vortex ring at which the bubbles are injected ($x = 0.5$ m), entrained ($x = 0.55$ m), settled ($x = 0.6$ m) and escape in the $\hat{z}$ direction ($x = 0.65$ m). Before bubble injection, the vorticity profile consists of mainly concentric iso-vorticity contours, as shown in figure 8(*a*,*b*). As the bubbles are injected and they become entrained into the ring, they begin to alter the vortex structure. As the bubble is entrained and passes through close to the vortex centre ($x = 0.55$ m, figure 8(*d*), it splits the high-vorticity region into smaller regions. Settled bubbles cause significant distortion in the vortex structure (figure 8*f*,*h*), not just in the local region of bubble motion, but within the entire core radius ($r_c = 0.011\,45$ m), an observation similar to the experimental data. The vortex core radius is the same as utilized in the experimental studies. The volume displacement effects present in the volumetric coupling cases were found to be important in predicting this behaviour. As is discussed later, this process of vortex core fragmentation was not observed using standard two-way coupling approaches even with the presence of bubbles. With two-way coupling, the vortex structure is very similar to the unladen case, indicating that the point-source momentum coupling alone is insufficient to affect the vorticity distribution within the core.

Figure 9 shows bubble escape characterized by the angle ϕ from the plane of injection and obtained by averaging over all bubbles in the vortex ring at $x = 0.65$ m, close to the end of the simulations. The scatter in radial distance from the centre of the vortex ring (R) is evident for cases with different vortex strengths. The degree of escape was found to be substantially larger in the volumetric coupling cases as compared to the two-way coupling, which confirms that the effect of bubbles on the vortex structure is driving this escape behaviour. For some cases, small-bubble escape was present even without the effects of vortex distortion, as bubbles can travel laterally across an undistorted vortex axis. However, the differences between the escape characteristics predicted by the two-way and volumetric coupling models can be mostly attributed to vortex distortion induced by volume displacement effects. It is conjectured that the bubble escape is dependent on the degree to which the bubbles have locally weakened the vortex, which can change with time. This vortex distortion

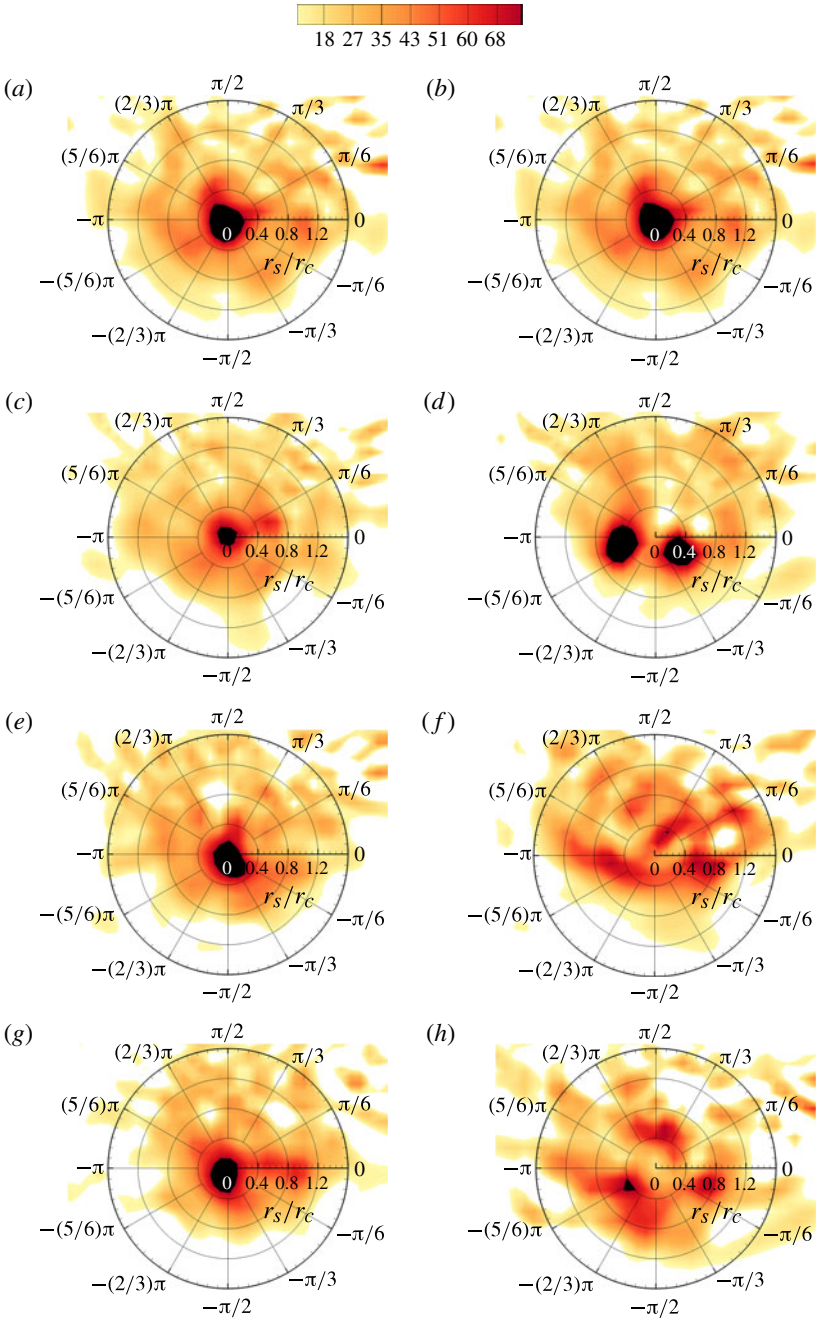

FIGURE 8. (Colour online) Temporal evolution of the out-of-plane vorticity in cylindrical coordinates for the weak vortex case no. 3, $\Gamma_0 = 0.0159$ m^2 s^{-1}. Panels (*a*), (*c*), (*e*), (*g*) are for the unladen case; panels (*b*), (*d*), (*f*), (*h*) are when eight bubbles of $d_b = 700$ μm are entrained; (*a*), (*b*) $x_c = 0.5$ m; (*c*), (*d*) $x_c = 0.55$ m; (*e*), (*f*) $x_c = 0.6$ m; (*g*), (*h*) $x_c = 0.65$ m. The time difference between each plot is approximately 0.4 s. The vorticity field has been filtered below $\omega_z < 10$ to show the high degree of distortion and core fragmentation.

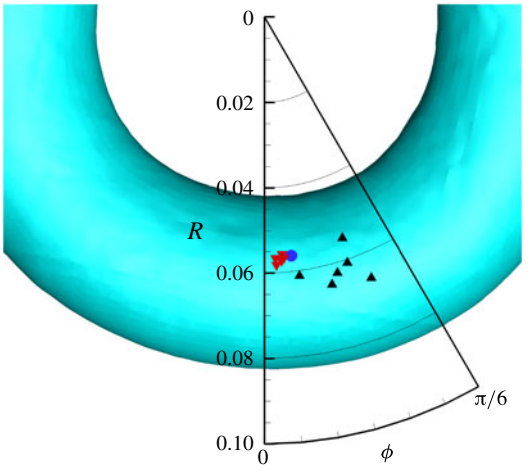

FIGURE 9. (Colour online) Bubble escape locations away from the plane of injection for the volumetric coupling simulations. Position indicated is the average location of the eight bubbles in each case when the vortex core centre reaches 0.65 m: $\Gamma_0 = 0.0159$ m^2 s^{-1} (▲); $\Gamma_0 = 0.207$ m^2 s^{-1} (●); $\Gamma_0 = 0.0254$ m^2 s^{-1} (▼).

is discussed in § 3.3. As shown in figure 8, large bubbles entrained in a weak vortex can fragment the vortex core, and hence the escape of the bubbles from the plane of injection is more likely and their positions more scattered. Although the bubble escape was observed in the experiments, it was not quantified or correlated to the vortex distortion. For the strong vortex cases, the distortions in the vortex structure are small and the bubbles are settled in relatively close proximity of each other (with minimal escape). However, for weak vortex cases, the bubbles show moderate to significant escape and are scattered further away from each other. This means that local variations in the liquid volume fraction will be reduced, and the distorted vortex core can begin to repair itself under certain conditions, as seen in the experimental observations of Sridhar & Katz (1999).

3.3. *Quantification of vortex distortion and its effects*

It is clear from the previous discussion that the fluid displacement effects are important in distorting the vortex and distributing the vorticity within the core. This can be further seen by inspecting the radial variation of azimuthally averaged vorticity for the unladen and bubble-laden case no. 5 (corresponding to the weak vortex strength of $\Gamma_0 = 0.0159$ m^2 s^{-1} and large bubbles $d_b = 1100$ μm) with different modelling techniques, as shown in figure 10. As shown before, this case exhibits significant escape of bubbles when the vortex ring reaches $x = 0.65$ m (figures 8*h* and 7*c*). Figure 8 shows that, on the plane of injection, the regions of peak vorticity are pushed outwards from the core centre due to the bubbles passing nearby. Once the bubbles settle further away from the core and slowly escape from the plane of injection, a different trend appears. With averages taken over the region of bubble escape, a consistent increase in the core centre vorticity was observed. This suggests that, as the bubbles move into planes other than the injection plane, they affect a much larger area of the ring. A core centre increase in vorticity was also found in the experiments by Sridhar & Katz (1999). It is also observed from these figures that the one-way and two-way profiles are very similar; the maximum variation in the averaged

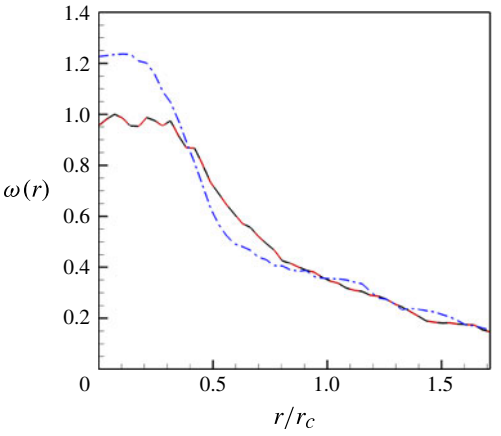

FIGURE 10. (Colour online) Radial variation of azimuthally averaged vorticity profiles for the weak vortex case of $\Gamma_0 = 0.0159$ m^2 s^{-1} for $d_b = 1300$ μm, corresponding to case no. 5: one-way, unladen case (—); two-way coupling (---; which cannot be distinguished from the previous curve); volumetric coupling (-·-·); average azimuthally as well as over different planes within a thickness of 0.004 m, representative of bubble escape.

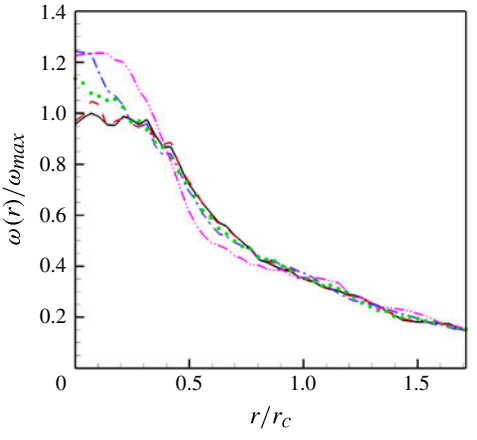

FIGURE 11. (Colour online) Radial variation of azimuthally averaged vorticity profiles, average taken over several planes within a thickness 0.004 m representative of bubble escape, for the weak vortex case of $\Gamma_0 = 0.0159$ m^2 s^{-1} using the volumetric coupling formulation: unladen case (—); 500 μm (---); 700 μm (-·-·); 900 μm (• • •); 1100 μm (-··-··).

vorticity is less than 1 % at any location within the domain. This indicates that, even for weak vortex strength and large bubbles, the point-source momentum coupling induced no effect on the flow structure, unlike that observed in the experiments.

Figure 11 compares the change in azimuthally averaged vorticity distribution when bubbles of different size are entrained in the weak vortex. In general, the core centre vorticity increase is larger as the size of the bubbles entrained is increased. It also shows that vorticity increases near the core centre, $r/r_c < 0.4$, and decreases further away from the core, $0.5 < r/r_c < 1$. In the strong vortex cases, these averaged vorticity profiles differed only marginally from the unladen cases.

Case no.	Cr ($\times 10^{-5}$ m)	$I_{0.4}$	I	Distortion
1	2.15	0.07	0.68	Minimal
2	8.85	0.26	1.63	Minimal
3	5.15	1.01	5.68	Moderate
4	10.65	0.71	4.15	Significant
5	46.15	2.54	11.8	Significant
6	53.15	1.92	8.77	Significant
7	7.2	0.71	2.1	Minimal
8	7.5	0.09	0.48	Minimal
9	3.75	0.23	1.10	Minimal
10	22.9	0.61	4.10	Moderate
11	20.9	0.62	4.02	Moderate
12	33.6	0.79	4.26	Moderate

TABLE 2. Quantification of vortex distortion using various measures.

In order to further quantify the degree of vortex distortion as a function of bubble size or bubble settling location, several measures can be used. Sridhar & Katz (1999) used two point measurements to characterize the vortex distortion, namely: (i) relative rise in peak vorticity within the vortex core; and (ii) relative rise in the vortex core centre (termed core rise C_r) due to bubble entrainment in comparison with the unladen case. Based on the amount of increase in the peak vorticity or core rise, they classified distortion into minimal, moderate and significant. They found that bubbles that settled in a band of $0.2 \leqslant r_s/r_c \leqslant 0.4$ showed moderate to significant distortion based on these criteria. In the present work, in addition to the core rise as the point measure, a global measure based on change in azimuthally averaged vorticity in the bottom plane for bubble-laden and unladen cases was computed and used to quantify vortex distortion. Accordingly, two measures are defined as

$$I_{0.4} = \frac{\int_0^{2\pi}\int_0^{0.4r_c} |\omega(r) - \omega(r)_{unladen}|\, r\,\mathrm{d}r\,\mathrm{d}\theta}{\Gamma_0} \times 100, \tag{3.6}$$

$$I = \frac{\int_0^{2\pi}\int_0^{1.71r_c} |\omega(r) - \omega(r)_{unladen}|\, r\mathrm{d}r\,\mathrm{d}\theta}{\Gamma_0} \times 100, \tag{3.7}$$

where ω and $\omega_{unladen}$ represent the local vorticity in the bubble-laden and unladen cases, respectively. Note that this measure can be obtained by using vorticity values in the plane of injection only or by averaging vorticity values over several planes in a region of certain thickness, corresponding to the bubble escape, around the plane of injection. The limits for radial integrations are based on the region containing the settled bubbles where an increase in average vorticity was obtained compared to the unladen case ($<0.4r_c$) or the entire radial region of vortex, not just the core. Both are normalized by the vortex strength, Γ_0.

Table 2 lists the values of these measures and accordingly quantifies the amount of distortion as minimal, moderate or significant. Moderate distortion was classified as having $I > 2.0$ and $Cr > 5.0 \times 10^{-5}$ m, significant distortion features $I > 4.0$ and $Cr > 10.0 \times 10^{-5}$ m. Anything less than moderate is classified as minimal distortion. Figure 12 shows a measure of vortex distortion (I) as a function of bubble settling

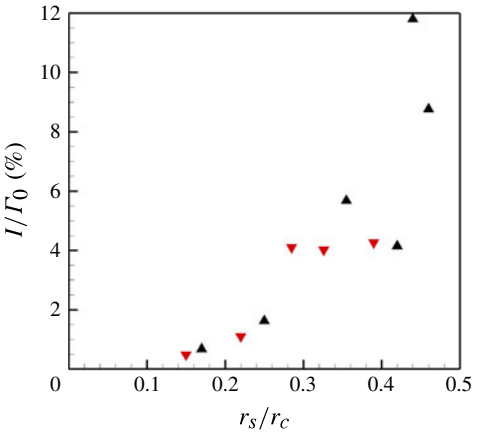

FIGURE 12. (Colour online) Variation of the vortex distortion measures versus bubble settling location for the weak (▲, $\Gamma_0 = 0.0159\ \mathrm{m^2\ s^{-1}}$) and strong (▼, $\Gamma_0 = 0.0254\ \mathrm{m^2\ s^{-1}}$) vortex cases.

location for the weak as well as strong vortex strengths. These measures indicate that, as bubbles settle further away from the vortex core, they strongly influence the vorticity distribution within the core. As discussed later, within injection of bubbles into the vortex ring, fluid is displaced locally through their presence and motion. The magnitude of fluid displacement and its impact on fluid momentum increases with r_s/r_c. The deformation to the vortex core increases with increased bubble size and final settling location. Note that these measures based on averaged vorticity within the region of bubble escape showed an increase in vortex distortion, even for bubbles that show significant escape as discussed in the previous paragraph.

3.4. *Wake effects*

The vortex distortion observed in some of the cases can be explained by investigating the bubble wakes. In the present volumetric coupling model, the complete wakes of the bubbles are not fully resolved because the bubbles are subgrid. However, the fluid displaced by the bubbles indeed captures the wake effects reasonably well. This can even be observed by looking at a simple rising bubble in a quiescent flow. The volumetric coupling model predicts a reasonable wake, whereas the the standard point-particle approach with two-way coupling does not lead to significant displacement of the fluid.

In studying the forces acting on interface-contaminated bubbles in a rotating flow, Rastello *et al.* (2009) noted three distinct regimes that led to varying levels of distortion in their vortices. Their experiment consisted of a single bubble being trapped in a solid-body rotating flow. Small bubbles that tend to settle close to the core centre had small enough Reynolds numbers, owing to both a low relative velocity and small diameter, that their wake had little effect on the mean flow. In some intermediate range, the bubble had a significantly strong wake so that the bubble would experience a distorted flow field; in turn compounding the effect. The largest bubbles will settle outside of this intermediate range. While they leave a large wake, it is not strong enough to travel around the vortex as that wake must travel a distance of $2\pi r_s$ in order for the bubble to experience it. Their work noted that the bubble wakes tended to wrap towards the centre of the vortex, as opposed to precisely following a streamline

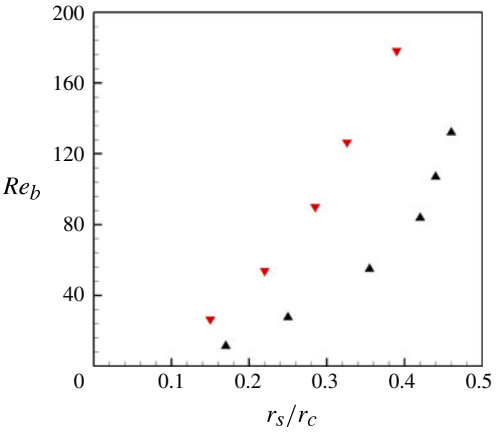

FIGURE 13. (Colour online) Bubble Reynolds number (Re_b^{ref}) versus non-dimensional bubble settling location for the weak (▲, $\Gamma_0 = 0.0159\ \mathrm{m^2\ s^{-1}}$) and strong (▼, $\Gamma_0 = 0.0254\ \mathrm{m^2\ s^{-1}}$) vortex cases.

(Rastello *et al.* 2009). Since the vortex was forced by the spinning cylinder, the wake was probably degraded strongly with time.

In the present work, it is postulated that the bubble wakes and their interaction with the centre of the vortex play a critical role in vortex distortion. In order to obtain an estimate of the nature of the bubble wake, the reference Reynolds number of the bubbles (Re_b^{ref}) is plotted versus the bubble settling location in figure 13. Here Re_b^{ref} is defined, with U_{rel} as the velocity scale and d_b as the length scale. It is important to note that the bubble settling location cannot be solely determined by the bubble Reynolds number. It is observed that, for both low as well as strong vortex strengths, the bubble Reynolds number increases with bubble settling location, which is further away from the vortex centre for larger bubbles. The bubble Reynolds numbers range over 20–160 for the cases studied, whereas for bubbles with settling location within $0.2 \leqslant \bar{r}_s \leqslant 0.4$ this range is between 30 and 90.

In general, for flow over a sphere, the wake tends to be steady and symmetric when the bubble Reynolds number is below 150, assuming the incoming flow is uniform. Between roughly 150 and 280 the wake is steady but asymmetric, and beyond 280 unsteadiness can set in (Ormières & Provansal 1999; Tomboulides & Orszag 2000; Mittal *et al.* 2008). For the ranges considered in this paper, if the flow experienced by a settled bubble was uniform, we would expect steady wakes with lengths and widths of the order of the bubble diameter (Mittal *et al.* 2008). However, in the present work, the vortices do not offer a uniform flow and the bubbles, as mentioned previously, circulate around a settling location, as opposed to actually remaining stationary. This will cause the wakes to be unsteady, even when the bubble Reynolds number is well under 280.

In the present case involving a travelling vortex ring, two of the regimes noted by Rastello *et al.* (2009) seem to occur. The smallest bubbles that settle closer to the vortex centre ($\bar{r}_s \leqslant 0.2$) have low bubble Reynolds numbers and thus lead to wakes that are too weak to distort the flow significantly. The wakes for these bubbles also span over a very small distance and do not reach the vortex centre. As the bubble sizes get larger, which causes the bubbles to settle further away from the vortex core, the wakes generated are stronger and have the potential to distort the vortex core,

which would place them in the intermediate regime observed by Rastello *et al.* (2009). Figures 11 and 12 show that the observed distortion characterized by (3.7) increases with bubble size for the entire range studied at a given vortex strength. It is sensible to view the vortex distortion as a competition between the natural inclination of the vortex structure to repair itself, as observed in Sridhar & Katz (1999), and the strength of the disturbances generated. Bubbles that settled within the range of $0.2 \leqslant \bar{r}_s \leqslant 0.4$ also remained in the plane of injection and showed little escape as shown in figure 9. They are thus more clustered together and show large vortex distortion.

It is also informative to compare the distortion index for the weak and the strong vortex cases. For the weak vortex, as the bubble size increases, their settling location increases, the bubble Reynolds numbers are larger and the vortex distortion observed is also large. For these cases, the bubbles also tend to escape more and thus any initial distortion is likely to dampen with time. For the strong vortex strength, the vortex distortion also increases with bubble size and settling location. However, the amount of distortion for the largest bubbles is smaller compared to the corresponding weak vortex cases. Thus, even though large bubbles in the strong vortex have a stronger wake (owing to a higher U_{rel} and d_b), the observed distortion is subject to a stronger damping in those cases. This suggests that the vortex distortion is a function of the bubble settling location as well as the vortex strength or the vortex Reynolds number, and this is indeed shown to be the case in the following section.

4. Quantifying the volume displacement effects

The results presented in § 3.2 demonstrated that a low volume fraction of low-Stokes-number bubbles can have a substantial effect on the carrier phase flow when volume displacement effects are included. With only the point-particle momentum-source model, that is, two-way coupling, the vortex-ring structure was very similar to an unladen case. It is thus important to quantify and investigate these volume displacement effects in order to understand the mechanisms that alter the vortex structures. First the effects on the forces experienced by the bubbles is quantified by obtaining probability mass functions for different forces and comparing them with the unladen and two-way coupling cases. Next, as derived in § 2.4, the effect of local variations in fluid volume fractions can be isolated by comparing the linear momentum equations with the two-way coupling counterpart. Equation (2.25) gives an expression for the volumetric coupling influences on the flow field. A few measures to quantify these effects are identified here that are used to discuss the importance of the volumetric coupling formulation for bubble-laden flows.

4.1. *Effect on bubble forces*

In order to investigate how the changes in the vortex flow structure affect bubble motion, the probability mass functions of the radial pressure, added mass and lift forces on the bubble are shown in figure 14 for the one-way, two-way and volumetric coupling formulations. The forces are normalized by the maximum absolute value among the three coupling methods, so changes in both the mean and maximum can be seen. It can be seen that the probability mass functions for these force variations are nearly identical for the unladen (one-way) case and bubble-laden case with two-way coupling. However, all forces show a broader distribution with volumetric coupling. Comparing the mean of the distributions between the volumetric and two-way coupling, the pressure and added mass forces indicate a smaller force exerted onto the bubble inward towards the core with the volumetric coupling formulation. The

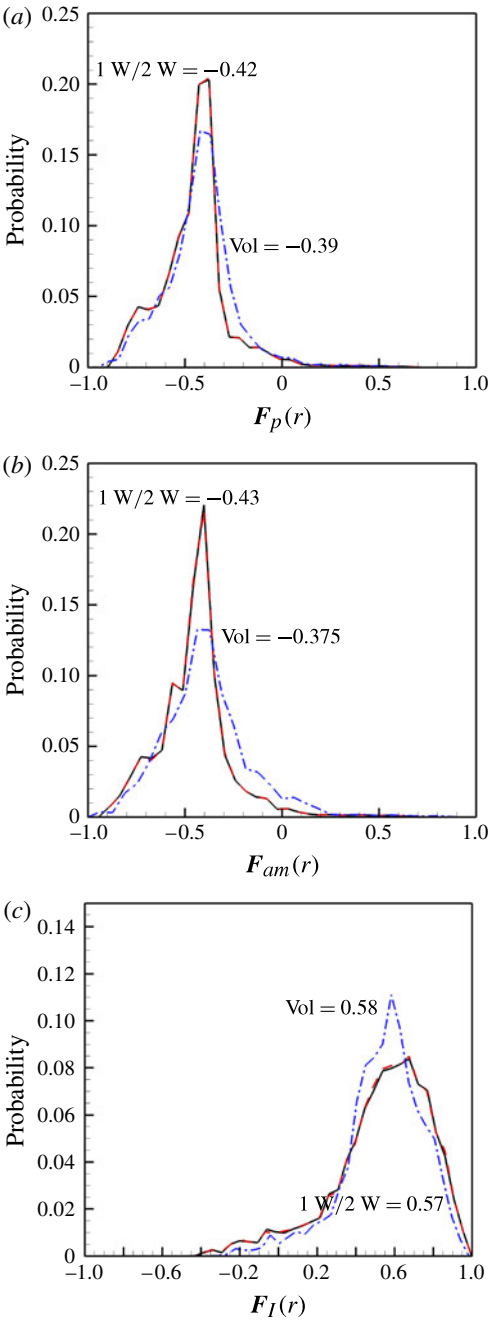

FIGURE 14. (Colour online) Probability mass functions for the radial components of forces on the bubble obtained in one-way (—), two-way (---) and volumetric coupling (-·-·) formulations for case no. 5: (*a*) radial pressure force; (*b*) radial added mass force; and (*c*) radial lift force, normalized by the maximum absolute value. Mean values of the forces are also given for one-way (or unladen), two-way and volumetric coupling methods.

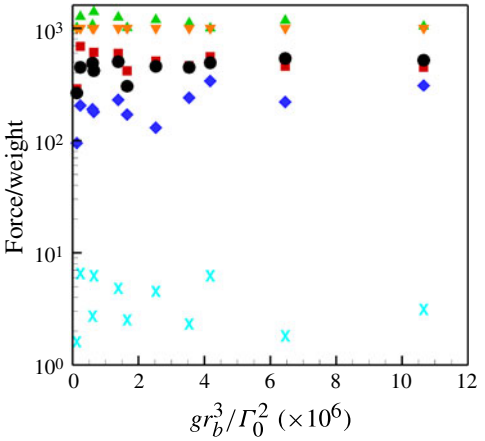

FIGURE 15. (Colour online) The magnitudes of individual forces on the bubbles (averaged over all bubbles) and normalized by the bubble weight for different cases on log-linear scale: drag (▲); dynamic pressure gradient (■); lift (●); added mass (♦); hydrostatic pressure gradient (▼); and summation of net force on the bubble (X).

mean pressure force decreased by 7.6 %, whereas the added mass force decreased by 12.8 %, while the lift force shows a larger force pushing outwards from the core centre, with an increase of 1.7 %. The effect on drag force was found to be very small. The combined effect of changes in these forces results in a radial settling location that is slightly further away when the volume displacement effects are considered. These modifications to bubble forces due to vortex distortion are found to be important to obtain the correct trend for settling locations as shown in figure 5.

4.2. *Two-way point-source versus volumetric coupling*

The individual contributions of different reaction terms in $\boldsymbol{f}^t_{b\to\ell}$ are computed on each bubble for the different cases studied. The *magnitudes* of forces (averaged over the $N_b = 8$ injected bubbles) are plotted against the gravity parameter gr_b^3/Γ_0^2 in figure 15. The forces are normalized by the bubble weight. The buoyancy force (or the hydrostatic pressure-gradient force, $\rho_\ell \mathscr{V}_b \boldsymbol{g}$) is close to 1000 times the weight of the bubble owing to the small specific gravity of the bubble. It is also observed that the magnitudes of individual drag, lift, added mass and pressure forces (due to dynamic pressure gradient) are large, and of the order of 300–1200 times the bubble weight. However, the net two-way reaction force, $\boldsymbol{f}^t_{b\to\ell}$, is found to be small and does not affect the vortex-ring structure in a two-way coupling formulation, even for the weak vortex case. This can be explained based on the balance of the forces on the bubbles.

If the bubbles settle perfectly at a location that remains stationary with respect to the vortex core, then the different forces acting on them are in perfect balance with their weight, that is,

$$(\boldsymbol{F}_d + \boldsymbol{F}_\ell + \boldsymbol{F}_{am} + \boldsymbol{F}_p) = -\boldsymbol{F}_g = \rho_b \mathscr{V}_b \boldsymbol{g}. \tag{4.1}$$

Owing to transitional flow in a vortex ring, the bubbles do not settle perfectly but continue to circle around a mean settling location. However, the net reaction force is still small in a two-way coupling formulation due to the small specific gravity of the bubbles. While these forces have components in all three directions, they are dominated by the components in the settling plane as shown in figure 3(*c*).

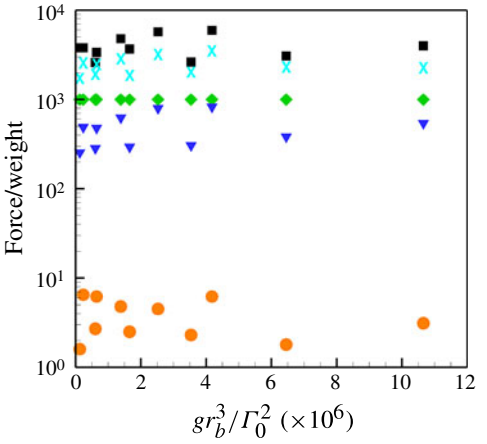

FIGURE 16. (Colour online) The magnitudes of individual volumetric coupling reaction forces (defined in (2.25)) normalized by the net bubble weight on log-linear scale. The forces are averaged in time after the bubbles are settled: unsteady and inertial terms, $\overline{\Delta V}_2$ (▼); two-way coupling momentum transfer term, $\overline{\Delta V}_1 + \overline{\Delta V}_4$ (●); hydrostatic buoyancy term, $\overline{\Delta V}_5$ (♦); local divergence term, $\overline{\Delta V}_6$ (■); and total magnitude of signed summation of the volume displacement forces, $\overline{\Delta V_{net}}$ (X).

Figure 16 shows the relative magnitudes of the various volumetric source terms obtained in (2.25). These magnitudes are obtained by accounting for the net sources on the fluid and averaging them over the period of time after the bubbles have settled around a mean position. The magnitudes are normalized by the net bubble weight and are given as

$$\overline{\Delta V_i} = \frac{\overline{\sum_{cv} |\widehat{\Delta \boldsymbol{V}_i}| \mathscr{V}_{cv}}}{W_b} = \frac{\overline{\sum_{cv} (\widehat{\Delta V}_{i_x}^2 + \widehat{\Delta V}_{i_y}^2 + \widehat{\Delta V}_{i_z}^2)^{1/2} \mathscr{V}_{cv}}}{N_b \rho_b \mathscr{V}_b g}, \tag{4.2}$$

where N_b is the number of bubbles, W_b is the weight of the bubbles, $\mathscr{V}_{cv}$ is the volume of the cell and the overbar represents time average. Also shown in figure 16 is the magnitude of the vector sum (signed sum) of the volume displacement forces normalized by the net bubble weight,

$$\overline{\Delta V_{net}} = \frac{\overline{\widehat{\Delta V_{net}}}}{W_b} = \frac{\overline{\sum_{cv} \left| \sum_{i=1}^{6} \widehat{\Delta \boldsymbol{V}_i} \right| \mathscr{V}_{cv}}}{N_b \rho_b \mathscr{V}_b g}. \tag{4.3}$$

It is observed that the individual magnitudes of the different volume displacement coupling forces are large, with the divergence-based reaction term ($\overline{\Delta V}_6$) being the largest in all cases. Since the local divergence in the flow field is related to the local spatio-temporal variations in the bubble volume fraction (see (2.13)), the effect of fluid displaced by the presence of bubbles can be significant. The summed magnitudes of two-way coupling forces, although large, are still smaller than this divergence reaction term. The forces here are roughly constant when normalized by the bubble weight for all gr_b^3/Γ_0^2, since both the volume displacement forces and the bubble weights

are proportional to the bubble volume. There are variations caused by the differences in the flow field seen by the bubbles due to their respective settling distances and bubble escape properties. The net magnitude of the vector summation of the volume displacement forces ($\overline{\Delta V_{net}}$) shows that the net addition is smaller than some of the individual components, and thus some of these effects are balancing each other. However, the net magnitude is still considerably larger than the net magnitude of the two-way coupled forces (which is close to the weight of the bubbles for settled bubbles). Thus, the volumetric coupling does impart a larger reaction force and can cause distortion of the vortex ring for certain cases.

4.3. *Comparing volume displacement forces to a simple two-dimensional estimate*

In previous two-dimensional work on bubble–vortex tube interactions (Finn *et al.* 2011), models have been developed to estimate an analogous expression for the volume displacement force. The reaction force was derived by directly subtracting the one-way coupled Navier–Stokes equation (4.4) from the volumetric coupling equation (2.14), shown again here for completeness in (4.5):

$$\underbrace{\frac{\partial(\rho_\ell \boldsymbol{u}_\ell)}{\partial t} + \boldsymbol{\nabla}\cdot(\rho_\ell \boldsymbol{u}_\ell \boldsymbol{u}_\ell)}_{\boldsymbol{C}} = \underbrace{-\boldsymbol{\nabla} p}_{\boldsymbol{P}} + \underbrace{\boldsymbol{\nabla}\cdot[\mu_\ell(\boldsymbol{\nabla}\boldsymbol{u} + \boldsymbol{\nabla}\boldsymbol{u}^T)]}_{\boldsymbol{V}} - \underbrace{\rho_\ell \boldsymbol{g}}_{\boldsymbol{B}}, \tag{4.4}$$

$$\underbrace{\frac{\partial(\rho_\ell \theta_\ell \boldsymbol{u}_\ell)}{\partial t} + \boldsymbol{\nabla}\cdot(\rho_\ell \theta_\ell \boldsymbol{u}_\ell \boldsymbol{u}_\ell)}_{\hat{\boldsymbol{C}}} = \underbrace{-\boldsymbol{\nabla} p}_{\hat{\boldsymbol{P}}} + \underbrace{\boldsymbol{\nabla}\cdot[\mu_\ell \theta_\ell(\boldsymbol{\nabla}\boldsymbol{u} + \boldsymbol{\nabla}\boldsymbol{u}^T)]}_{\hat{\boldsymbol{V}}} - \underbrace{\rho_\ell \theta_\ell \boldsymbol{g}}_{\hat{\boldsymbol{B}}} + \boldsymbol{f}^t_{b\to\ell}. \tag{4.5}$$

This expression is in general agreement with those given by Druzhinin & Elghobashi (1998) and Sridhar & Katz (1999) for similar bubble-laden systems. Subtracting the previous two equations gives

$$\widehat{\Delta \boldsymbol{R}} = (\boldsymbol{C} - \hat{\boldsymbol{C}}) + (\hat{\boldsymbol{P}} - \boldsymbol{P}) + (\hat{\boldsymbol{V}} - \boldsymbol{V}) + (\hat{\boldsymbol{B}} - \boldsymbol{B}) + \boldsymbol{f}^t_{b\to\ell}. \tag{4.6}$$

To obtain a simple two-dimensional estimate of the reaction force, the differences in the convective, viscous, pressure, buoyancy and two-way coupling momentum transfer terms, shown in (4.6), can be approximated using a Gaussian vortex profile (based on the nature of the averaged vorticity distribution shown in figure 10) under the assumptions of an undisturbed flow field and zero bubble acceleration (or assuming that the forces on bubbles are in balance), which provides good estimates for velocity, vorticity and dynamic pressure gradient at all positions in the vortex core. The resultant $\widehat{\Delta \boldsymbol{R}}$ is non-zero because, under the two-way coupling model, convective and buoyancy effects are not weighted by the actual local fluid volume fraction, whereas under the volumetric coupling model these terms are weighted by the actual amount of fluid present. The reasoning here is equivalent to that which was used to find $\widehat{\Delta \boldsymbol{V}}$ in § 2.4. The individual terms in (4.6) can then be simplified by neglecting the viscous terms (for low volume loadings and large Re_{vx}) as (Finn *et al.* 2011)

$$\boldsymbol{C} - \hat{\boldsymbol{C}} = \rho_\ell \frac{\mathrm{D}\boldsymbol{u}_\ell}{\mathrm{D}t} - \frac{\mathrm{D}\,(\rho_\ell \theta_\ell \boldsymbol{u}_\ell)}{\mathrm{D}t} \approx \rho_\ell \frac{u_\theta^2}{r} - \rho_\ell \frac{\theta_\ell u_\theta^2}{r} \approx \rho_\ell \theta_b \frac{u_\theta^2}{r}, \tag{4.7}$$

$$\hat{\boldsymbol{B}} - \boldsymbol{B} = -\theta_\ell \rho_\ell \boldsymbol{g} + \rho_\ell \boldsymbol{g} = +\theta_b \rho_\ell \boldsymbol{g}. \tag{4.8}$$

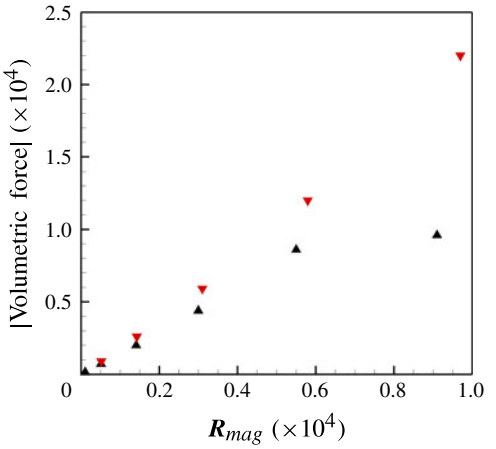

FIGURE 17. (Colour online) Comparison of the net volume displacement force obtained in present three-dimensional computations to the two-dimensional estimate based on a simplified Gaussian vortex of similar strength for the weak (▲, $\Gamma_0 = 0.0159\ \mathrm{m^2\ s^{-1}}$) and strong (▼, $\Gamma_0 = 0.0254\ \mathrm{m^2\ s^{-1}}$) cases.

Also, assuming that the bubbles reach a settling location that is steady with respect to the vortex core, the net forces on the bubble are in balance,

$$\boldsymbol{F}_{b\to\ell} = -(\boldsymbol{F}_d + \boldsymbol{F}_\ell + \boldsymbol{F}_{am} + \boldsymbol{F}_p) \sim \boldsymbol{F}_g = -\rho_b \mathscr{V}_b \boldsymbol{g}, \tag{4.9}$$

$$\boldsymbol{f}^t_{b\to\ell} \sim \sum_{b=1}^{N_b} \mathscr{G}_\Delta(\boldsymbol{F}_{b\to\ell}) = -\theta_b \rho_b \boldsymbol{g}. \tag{4.10}$$

Note that the interphase reaction term will be small when the bubbles are not accelerating, explaining why the point-particle, two-way coupling source causes almost no vortex distortion. If all terms in (4.8) and (4.10) are combined, and multiplied through by the local volume of the fluid cell, then the two-dimensional approximation to the total reaction force ($\Delta\boldsymbol{R} = \mathscr{V}_{cv}\widehat{\Delta\boldsymbol{R}}$) onto the fluid because of N_b bubbles having volume $\mathscr{V}_b$ can be obtained. The radial and tangential components (radially outwards and anticlockwise being positive) of this force are given as

$$R_r = -N_b \mathscr{V}_b(\rho_\ell u_\theta^2/r_s - g(\rho_\ell - \rho_b)\sin(\theta_s)), \tag{4.11}$$

$$R_\theta = N_b \mathscr{V}_b g(\rho_\ell - \rho_b)\cos(\theta_s), \tag{4.12}$$

$$R_{mag} = \sqrt{R_r^2 + R_\theta^2}, \tag{4.13}$$

where R_{mag} denotes the net magnitude of these two components. Note that (4.13) indicates that the two-dimensional estimate of the interaction force varies with the bubble volume. Figure 17 compares the volume displacement force magnitudes directly computed in this work ($|\widehat{\Delta\boldsymbol{V}_{net}}|$) to the prediction based on the stationary two-dimensional model (R_{mag}). For the strong vortex cases, where the vortex distortion is minimal and the bubbles tend to settle close to each other, the present computational prediction of the volume displacement force is directly correlated with the two-dimensional estimate. For these cases, the bubble escape observed in the computations was minimal and the steady two-dimensional assumption seems valid. For the weak

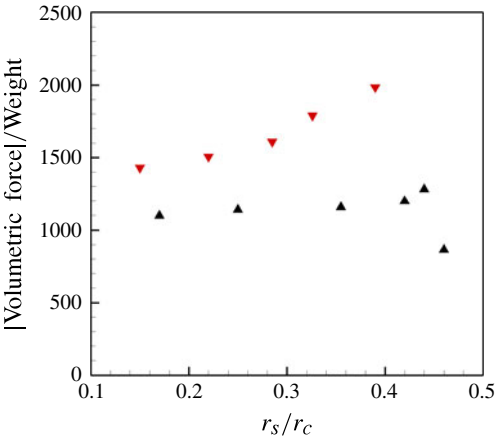

FIGURE 18. (Colour online) The resultant volume displacement force ($\widehat{\overline{\Delta V_{net}}}$) normalized by the net bubble weight for the weak (▲, $\Gamma_0 = 0.0159\ \mathrm{m^2\ s^{-1}}$) and strong (▼, $\Gamma_0 = 0.0254\ \mathrm{m^2\ s^{-1}}$) vortex cases, versus the mean non-dimensional settling location (r_s/r_c).

vortex, however, the forces tend to deviate from a direct correlation. The three-dimensional vortex distortion effects, bubble escape and unsteady nature of the bubble–vortex interactions were important for these cases.

4.4. *Volume displacement force and vortex distortion*

In order to study the influence of the net volume displacement force ($\overline{\Delta V_{net}}$) on the vortex structure and other forces acting on the bubble, it is first non-dimensionalized by the net bubble weight and plotted against the non-dimensional bubble settling location, $\bar{r}_s$, in figure 18. The weak and strong vortex cases are identified for comparison. It is observed that, for the strong vortex case, as the bubbles settle further away from the vortex core, the net volume displacement force is large. This is also the trend for the majority of the bubbles with the weak vortex, except for two cases where the bubbles settle further away from the core, where the normalized reaction force is lower. The magnitudes of these forces are larger for the strong vortex cases compared to the weaker vortex. These two effects can be explained as follows. For the strong vortex, the bubbles tend to settle in close proximity to each other with little or no escape, increasing the local spatial gradient in the bubble volume fraction. This increases the local divergence term and hence the local volume displacement effects. They also tend to move more rapidly because of the larger circulation rates. For the weaker vortex, on the other hand, the bubbles continue to move in small circles around a mean settling location and generally are more dispersed. They also show significant bubble escape from the plane of injection as shown in figures 7 and 9. These combined effects tend to have relatively lower net volume displacement forces for the weaker vortex. However, it is observed in the experiments as well as in the simulations that the large bubbles distort the weaker vortex significantly more compared to the strong vortex. To explain the effect of volume displacement forces on the vortex distortion, it is important to compare the volume displacement force to some measure of the vortex strength.

The volume displacement force can be normalized by the radial hydrodynamic pressure force within an undisturbed vortex core, which scales as $\rho_\ell \Gamma_0^2$ (which was

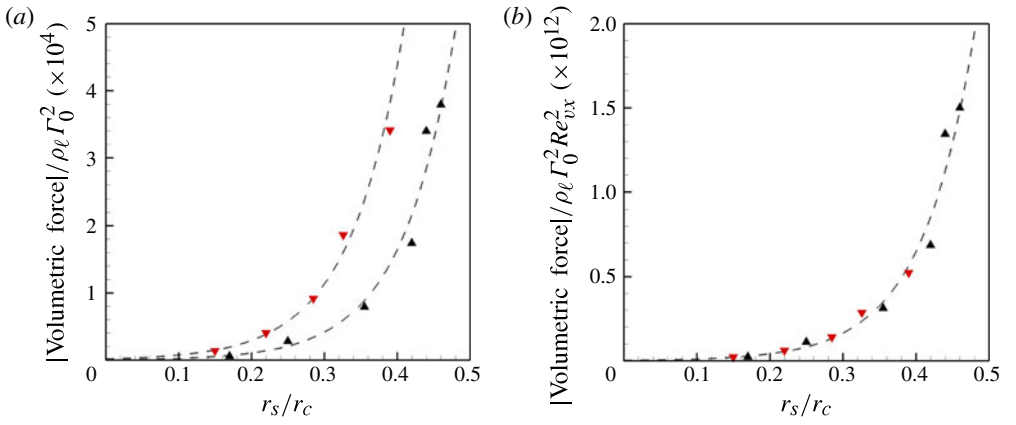

FIGURE 19. (Colour online) The net volume displacement force ($\overline{\widehat{\Delta V_{net}}}$) as a function of the mean settling location, r_s/r_c, for the weak (▲, $\Gamma_0 = 0.0159\ \mathrm{m^2\ s^{-1}}$) and strong (▼, $\Gamma_0 = 0.0254\ \mathrm{m^2\ s^{-1}}$) vortex strengths: (*a*) normalized by the net radial hydrodynamic pressure force in an undisturbed vortex ($\rho_\ell \Gamma_0^2$); and (*b*) normalized by $\rho_\ell \Gamma_0^2 Re_{vx}^2$.

also used to non-dimensionalize the bubble weight to obtain $\bar{g}$). The variation of this normalized force against the settling location, $\bar{r}_s$, is shown in figure 19(*a*). Two distinct trend curves arise from this normalization, indicating that the bubbles tend to settle further away for the weak vortex as compared to the large vortex. Note that the relationship of this normalized force with respect to the settling location for weak as well as strong vortex strengths is not linear. Since variation of the vortex strengths results in different vortex Reynolds numbers, $Re_{vx} = \Gamma_0/\nu_\ell$, it is then reasonable to assume that the normalized volume displacement force depends on Re_{vx}. The trend tends to collapse well when the net volume displacement force is normalized by the net hydrodynamic pressure force times the vortex Reynolds number squared, $\rho_\ell \Gamma_0^2 Re_{vx}^2$, as shown in figure 19(*b*). This plot shows that, as the bubbles tend to settle further away for the weak vortex, the normalized force is larger compared with the corresponding cases for the strong vortices. This plot thus indicates that the potential of the bubbles to distort the vortex ring is large for the weaker vortex, and hence significant distortion of the ring is observed for these cases. The volume displacement forces thus are given as

$$\frac{\overline{\widehat{\Delta V_{net}}}}{\rho_\ell \Gamma_0^2} = Re_{vx}^2 \mathscr{F}(\bar{r}_s), \tag{4.14}$$

where $\mathscr{F}$ is a nonlinear function of the settling location ($\bar{r}_s$). In addition, it was previously shown that the settling location depends on the ratio of the bubble weight to the hydrodynamic pressure force, $\bar{g} = g r_b^3/\Gamma_0^2$. It is important to note that the drag and lift forces acting on the bubble implicitly depend on bubble Reynolds number Re_b, which in turn depends on Re_{vx}. The bubble Reynolds numbers do not vary appreciably for the present case and hence the dependence of the drag and lift forces on vortex Reynolds number is weak. However, it is observed that the volume displacement forces, when normalized by Re_{vx}^2 and the hydrodynamic pressure force ($\rho_\ell \Gamma_0^2$), are direct functions of the settling location and collapse the data onto a single curve. This

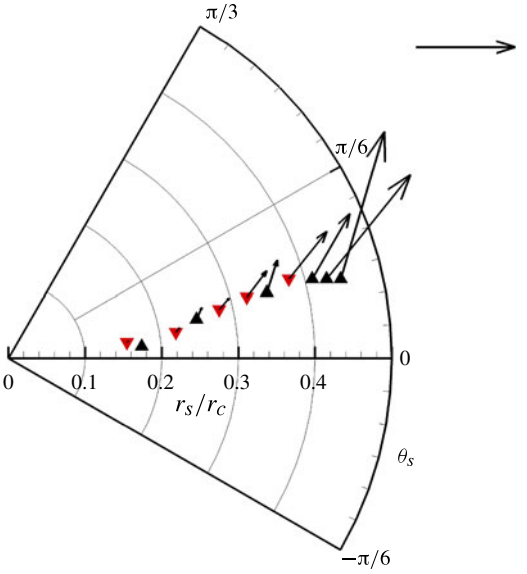

FIGURE 20. (Colour online) The normalized resultant volume displacement force ($\widehat{\overline{\Delta V_{net}}}/\rho_\ell \Gamma_0^2 Re_{vx}^2$) at different mean settling locations for strong (▼, $\Gamma_0 = 0.0254\ \mathrm{m^2\ s^{-1}}$) and weak (▲, $\Gamma_0 = 0.0159\ \mathrm{m^2\ s^{-1}}$) vortices. Arrow length represents 1×10^{-12} dimensionless units.

indicates that the vortex distortion occurring due to the fluid volume displaced by the bubbles is a function of Re_{vx} and gr_b^3/Γ_0^2.

In order to understand the directionality of the normalized net volume displacement force ($\overline{\Delta V_{net}}/\rho_\ell \Gamma_0^2 Re_{vx}^2$), it is plotted in the r_s–θ_s coordinates together with the location of the settled bubbles as shown in figure 20. The arrow denotes the directionality of the net force and the magnitude is represented by its length. It is observed that, for the weak as well as the strong vortex cases, as the bubbles settle further away from the vortex core, the net volume displacement force is also large. The resultant reaction force is still large for these cases. It is noticed from these plots that the resultant volume displacement forces are aligned roughly at 45° from the horizontal. Present computational results as well as experimental data (Sridhar & Katz 1999) indicate a core elongation at roughly 45° incline from the horizontal for cases in which significant distortion occurs. This approximate angle at which the core elongation occurs is the result of a competition between two mechanisms, the natural inclination of the vortex to have a horizontal elongation owing to its travelling nature, and the influence of the bubbles attempting to push the core to a more vertically inclined angle, shown in figure 20. The effect of fluid displaced by the bubbles is to locally elongate the flow structure near the centre of the vortex core. It is also important to note that in a steady flow a wake will develop at an angle of 180° relative to the net force reaction force on the fluid ($\widehat{\Delta \boldsymbol{V}}$). Based on the resultant direction of the volume displacement force shown in figure 20, the bubble wakes are directed inwards (or towards the vortex centre), similar to the observations by Rastello *et al.* (2009) based on their work on a forced vortex.

Finally, the vortex distortion index (I) defined in (3.7) is plotted against the normalized volume displacement force in figure 21. This plot clearly shows that

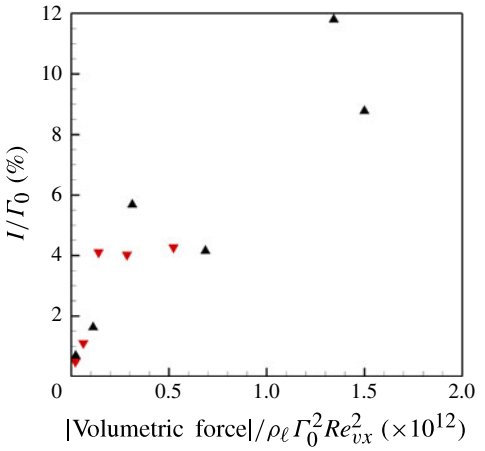

FIGURE 21. (Colour online) The vortex distortion index (I) versus the normalized resultant volume displacement force ($\widehat{\overline{\Delta V}_{net}}/\rho_\ell \Gamma_0^2 Re_{vx}^2$) for strong (▼, $\Gamma_0 = 0.0254$ m^2 s^{-1}) and weak (▲, $\Gamma_0 = 0.0159$ m^2 s^{-1}) vortex cases.

increase in volume displacement force increases the vortex distortion. Since the volume displacement force contains a major contribution from the local divergence term in the velocity field, then vortex distortion increases as the bubbles displace the fluid locally. As larger bubbles tend to displace more fluid and also settle further away from the vortex core, vortex distortion increases with increase in bubble settling location as shown previously in figure 12. Here it is shown that the vortex distortion index is correlated to volume displacement force, which also increases with bubble settling location.

4.5. *A simple modification to point-source momentum coupling*

To account for the volumetric displacements, the formulation presented here involves modification to the continuity and momentum equations. The fluid flow solver algorithm has to be modified considerably to account for the local variations in volume fractions and a variable-density-like pressure-based formulation is needed. The pressure Poisson equation has a source term due to variations in the local volume fractions and the flow field is no longer divergence-free. This can cause convergence issues in regions of large variations in volume fractions or for densely loaded systems.

A simplified approach that retains some of the main features of the volumetric coupling can be obtained for dilute loadings such that considerable changes to the basic incompressible flow solver are not needed. If the size of the dispersed phase is assumed small compared to the grid size (as in the cases studied in this work), the volume displacement force in the momentum equation (2.23) can be accounted for as a volumetric source term in the momentum equation, in addition to the two-way coupling point source. The cost associated with incorporating these additional source/sink terms along with the two-way coupling reaction force is negligible, and this model presents an effective alternative to incorporate some of the effects associated with the finite size of the dispersed phase in a point-particle approach.

Starting with (2.23), dividing throughout by θ_ℓ, expanding the viscous term using the product rule, and subtracting from this the one-way coupling equation (2.24) with a

volumetric source term ($\widehat{\Delta \boldsymbol{V}}$), we get

$$\widehat{\Delta \boldsymbol{V}} = \frac{1}{\theta_\ell}\boldsymbol{f}_{b\to\ell} + \rho_\ell(\boldsymbol{u}_\ell \boldsymbol{\nabla}\cdot\boldsymbol{u}_\ell) + \frac{1}{\theta_\ell}(\mu_\ell(\boldsymbol{\nabla}\boldsymbol{u}_\ell + \boldsymbol{\nabla}\boldsymbol{u}_\ell^T))\cdot\boldsymbol{\nabla}\theta_\ell \tag{4.15}$$

$$= \frac{1}{\theta_\ell}\boldsymbol{f}_{b\to\ell} - \frac{\rho_\ell \boldsymbol{u}_\ell}{\theta_\ell}\left(\frac{\partial\theta_\ell}{\partial t} + \boldsymbol{u}_\ell\cdot\boldsymbol{\nabla}\theta_\ell\right) + \mu_\ell(\boldsymbol{\nabla}\boldsymbol{u}_\ell + \boldsymbol{\nabla}\boldsymbol{u}_\ell^T)\cdot\frac{1}{\theta_\ell}\boldsymbol{\nabla}\theta_\ell, \tag{4.16}$$

$$= \underbrace{\frac{1}{\theta_\ell}\boldsymbol{f}_{b\to\ell}}_{\text{I}} \underbrace{- \rho_\ell \boldsymbol{u}_\ell \frac{\mathrm{D}}{\mathrm{D}t}(\ln\theta_\ell)}_{\text{II}} + \underbrace{\mu_\ell(\boldsymbol{\nabla}\boldsymbol{u}_\ell + \boldsymbol{\nabla}\boldsymbol{u}_\ell^T)\cdot\boldsymbol{\nabla}(\ln\theta_\ell)}_{\text{III}}, \tag{4.17}$$

where the velocity divergence is replaced by the material rate of change of the fluid volume fraction from the continuity equation (2.13).

This shows that the volume displacement forces can be obtained by simply dividing the two-way coupling momentum point source by the local fluid volume fraction (term I), and adding two additional volumetric sources based on the local variations in the fluid volume fractions (terms II and III). The term II involves the local temporal and spatial variations in the volume fractions caused by motion of the bubbles. The third term represents modification of the viscous effects due to local variations in the volume fraction. For high Reynolds numbers, this viscous effect may be small compared to the other terms and may be neglected. Note that the last two terms are written as derivatives of the logarithm of the volume fraction. Owing to the Lagrangian nature of the bubbles, the source terms due to volume fraction variations can vary rapidly from one cell to another. Derivatives of the logarithm of the volume fraction will be smoother compared to the derivatives of the volume fraction field itself. The standard Lagrangian point-particle approach can now be easily modified by modelling the net reaction source in this way. If the effects of bubbles on the continuity equation are neglected, the basic fluid flow solver used in these approaches will remain unchanged.

The above equation indicates that, for small bubbles ($d_b/\Delta_{cv} \ll 1$, $\theta_\ell \to 1$), the variations in the local volume fractions will be small and terms II and III will be negligible. The standard two-way coupling point source is then recovered in a consistent manner. Depending upon the application, the dominant reaction term could be because of the net acceleration of bubbles (term I) or displacement of the fluid due to bubble motions (term II). This may in general depend on the dispersed-phase volume loading, the particle Stokes number, particle-to-fluid density ratio, the flow Reynolds number, orientation of gravity, and boundary conditions/effects.

For denser-than-fluid particle systems where the particle-to-fluid density ratio is small (for example, sediment transport, liquid fluidized beds and risers, etc.), the volumetric displacement effects can be large compared to the standard two-way point source. Even for large density ratios, in regions where the subgrid particles are nearly in equilibrium with the fluid (reached terminal velocity), such as in the near-wall region, the volume displacement effects may become important, and should be considered.

The volumetric coupling effects give rise to a variable-density-like formulation in an incompressible fluid solver (§ 2); the actual implementation of the approach is not completely straightforward. Hence, the simplified approach as presented here introduces an effective volumetric coupling force, which can be thought of as an improvement over the standard point-particle two-coupling force, which in part addresses the finite size of the particle. From that perspective, this model is indeed

attractive and straightforward to implement. It presents an area for future research to investigate its validity and suitability for different flow configurations.

5. Conclusions

In this work, direct numerical simulation utilizing point-particle Lagrangian bubble tracking was performed to study interactions of a few small bubbles with a travelling vortex ring, corresponding to the experimental set-up of Sridhar & Katz (1999). Two approaches modelling the effects of bubbles on the vortex ring were studied: (i) two-way coupling; and (ii) volumetric coupling. In both approaches, the bubbles are considered subgrid and only the centres of the bubbles are tracked by modelling the forces on the bubbles through drag, lift, pressure, added mass and gravity. In the traditional two-way coupling approach, the effect of the bubbles on the flow was modelled through momentum point sources based on the net reaction of forces exerted on the bubble by the fluid. In volumetric coupling, in addition to this momentum point source, the local variations in the bubble (or fluid) volume fractions are accounted for by modifying the continuity and momentum equations. With this formulation, the velocity field is no longer divergence-free even in an incompressible fluid owing to the presence of discrete bubbles.

The two approaches were used to study bubble–ring interactions by varying both the bubble size ($300 \leqslant d_b \leqslant 1300$) and the vortex strengths ($\Gamma_0 = 0.0159,\ 0.0207,\ 0.0254\ \mathrm{m^2\ s^{-1}}$). It was found that the two-way coupling point-particle approach was insufficient to reproduce the experimental observations for bubble settling location, bubble escape properties, vortex core deformation and core fragmentation even with the use of experimentally determined lift coefficients (Sridhar & Katz 1999). The volumetric coupling approach performed well in reproducing these observations for both the bubble and liquid phases. It was shown that, even for low volume loadings, a small number of bubbles entrained in a vortex ring can significantly alter the vortex core for certain combinations of the vortex strengths and bubble sizes. The bubbles were able to fragment the vortex core so as to increase the vorticity at the core centre, similar to experimental observations. For the weak vortex strength, the entrained bubbles also escape from the plane of injection along the vortex ring, with the larger bubbles showing more escape. The distortion of the vortex ring was found to be significant for the weak vortex case, when bubbles of medium size were entrained between 20 and 40 % of the core radius. Bubbles that are entrained too close to the vortex core resulted in significantly less distortion.

The distortion of the vortex structure caused by bubbles is attributed to the fluid volume displacement due to bubble motion. The bubbles, once entrained in the vortex ring, nearly settle at a mean position away from the vortex core, owing to the balance between the drag, lift, pressure and added mass forces. Once settled, the bubbles do not experience any appreciable acceleration to exert a strong momentum coupling force and thus the point-source two-way coupling model does not affect the vortex-ring structure. It was shown that the local displacement of the fluid due to bubbles tends to alter the vortex-ring structure, distorting it completely for certain cases. These volume displacement effects were found to be critical in reproducing experimental observations. It has been postulated that these volume displacement effects are required in order to model the effects of the wake trailing a bubble. The wake characteristics are critical in determining whether significant distortion of the vortex will occur, or if it will stay nearly unperturbed. The directionality of these

volume displacement effects was also well correlated to experimental observation of wake propagation in a rotating flow.

A method for isolating volume displacement effects was derived in detail from the momentum equations by introducing the notion of a volume displacement force on the fluid. This force was shown to have contributions from the local pressure gradient, the unsteady and inertial terms, viscous terms due to local variations in the fluid volume fraction, the interphase momentum exchange, the hydrostatic force, and the local flow divergence due to the volume displaced by the bubbles. The magnitudes of these individual forces were compared with the individual forces on the bubble, namely, drag, lift, added mass and pressure, to show that they were of the same order; however, the net contribution was also large, unlike the balance among the forces on the bubble. The contribution due to the flow divergence was found to be the most dominant mechanism in distorting the vortex core. The volumetric force was also compared with an analytical estimate of this force based on a two-dimensional symmetric Gaussian vortex to show good correlation for the strong as well as weak vortices, which showed minimal bubble escape from the plane of injection. For cases with large distortion of the vortex core, the three-dimensional bubble escape and unsteady effects were found to be important.

The volume displacement forces, when non-dimensionalized by the measure of hydrodynamic pressure force ($\rho_\ell \Gamma_0^2$), showed a direct dependence on the non-dimensional bubble settling location, r_s/r_c, as well as the vortex Reynolds number, $Re_{vx} = \Gamma_0/\nu_\ell$. The reaction force normalized by $\rho_\ell \Gamma_0^2 Re_{vx}^2$ collapsed onto a single curve showing strong correlation with the settling location. The magnitude of the normalized reaction force increased monotonically with the bubble settling location, indicating that the volume displacement effects, and hence vortex distortion potential, were large if the bubbles settled further away from the vortex core. The direction of the net resultant force was found to be aligned at roughly 45° in the bubble settling plane, r_s–θ_s, which explains the elongation of the vortex core, as seen in experimental results and this work, in this direction.

This work has established the need for the inclusion of the volume displacement effects, due to motion of a disperse phase even for dilute volume loading, to model the two-phase interactions properly. It is shown that, for subgrid particles where the finite-size effects are important but conducting fully resolved simulations is not realistic ($0.1 < d_b/\Delta_{cv} < 1$ and $St_b > 0.1$), accounting for local variations in bubble volume fractions can provide a practical and improved approach to standard two-way point-particle method. A simplified model, modifying the standard two-way coupling reaction force by including the volume displacement effects, was developed for disperse two-phase flows that includes contributions from the two approaches in a consistent manner.

Acknowledgements

Financial support from DoE's National Energy Technology Laboratory (URS Contract Number 41817M4077) and National Science Foundation under the grant NSF-CBET #1133363 is highly appreciated. The simulations were performed on the high-performance computing cluster at Oregon State University as well as at the Texas Advanced Computing Center's Lonestar. We also thank all reviewers for their constructive comments.

REFERENCES

APTE, S. V., MAHESH, K. & LUNDGREN, T. 2008 Accounting for finite-size effects in simulations of disperse particle-laden flows. *Intl J. Multiphase Flow* **34** (3), 260–271.

APTE, S. V., MAHESH, K., MOIN, P. & OEFELEIN, J. C. 2003 Large-eddy simulation of swirling particle-laden flows in a coaxial-jet combustor. *Intl J. Multiphase Flow* **29** (8), 1311–1331.

ARMENIO, V. & FIOROTTO, V. 2001 The importance of the forces acting on particles in turbulent flows. *Phys. Fluids* **13** (8), 2437–2440.

BALACHANDAR, S. 2009 A scaling analysis for point particle approaches to turbulent multiphase flows. *Intl J. Multiphase Flow* **35** (9), 801–810.

BALACHANDAR, S. & EATON, J. K. 2010 Turbulent dispersed multiphase flow. *Annu. Rev. Fluid Mech.* **42** (1), 111–133.

BLUEMINK, J. J., LOHSE, D., PROSPERETTI, A. & VAN WIJNGAARDEN, L. 2009 Drag and lift forces on particles in a rotating flow. *J. Fluid Mech.* **643**, 1–31.

CECCIO, S. L. 2010 Friction drag reduction of external flows with bubble and gas injection. *Annu. Rev. Fluid Mech.* **42** (1), 183–203.

DARMANA, D., DEEN, N. G. & KUIPERS, J. A. M. 2006 Parallelization of an Euler–Lagrange model using mixed domain decomposition and a mirror domain technique: application to dispersed gas–liquid two-phase flow. *J. Comput. Phys.* **220** (1), 216–248.

DENG, R., WANG, C.-H. & SMITH, K. 2006 Bubble behaviour in a Taylor vortex. *Phys. Rev.* E **73** (3), 036306.

DRUZHININ, O. A. & ELGHOBASHI, S. 1998 Direct numerical simulations of bubble-laden turbulent flows using the two-fluid formulation. *Phys. Fluids* **10** (3), 685–697.

ELGHOBASHI, S. 1991 Particle–laden turbulent flows: direct simulation and closure models. *Appl. Sci. Res.* **48** (3–4), 301–314.

ELGHOBASHI, S. 1994 On predicting particle-laden turbulent flows. *Appl. Sci. Res.* **52** (4), 309–329.

ELGHOBASHI, S. 2006 An updated classification map of particle-laden turbulent flows. In *IUTAM Symposium on Computational Approaches to Multiphase Flow*, vol. 81, pp. 3–10. Springer.

FERRANTE, A. & ELGHOBASHI, S. 2005 Reynolds number effect on drag reduction in a microbubble-laden spatially developing turbulent boundary layer. *J. Fluid Mech.* **543** (1), 93–106.

FERRANTE, A. & ELGHOBASHI, S. 2007*a* On the accuracy of the two-fluid formulation in direct numerical simulation of bubble-laden turbulent boundary layers. *Phys. Fluids* **19** (4), 045105.

FERRANTE, A. & ELGHOBASHI, S. 2007*b* On the effects of microbubbles on Taylor–Green vortex flow. *J. Fluid Mech.* **572**, 145–177.

FERRY, J. & BALACHANDAR, S. 2001 A fast Eulerian method for disperse two-phase flow. *Intl J. Multiphase Flow* **27** (7), 1199–1226.

FEVRIER, P., SIMONIN, O. & SQUIRES, K. D. 2005 Partitioning of particle velocities in gas–solid turbulent flows into a continuous field and a spatially uncorrelated random distribution: theoretical formalism and numerical study. *J. Fluid Mech.* **533**, 1–46.

FINN, J., SHAMS, E. & APTE, S. V. 2011 Modelling and simulation of multiple bubble entrainment and interactions with two-dimensional vortical flows. *Phys. Fluids* **23** (2), 023301.

GATIGNOL, R. 1983 Faxen formulae for a rigid particle in an unsteady non-uniform stokes flow. *J. Méc. Théor. Appl.* **1** (2), 143–160.

GIDASPOW, D. 1994 *Multiphase Flow and Fluidization: Continuum and Kinetic Theory Descriptions*. Academic Press.

GLEZER, A. 1988 The formation of vortex rings. *Phys. Fluids* **31** (12), 3532.

HARPER, J. 1972 The motion of bubbles and drops through liquids. In *Advances in Applied Mechanics*, vol. 12, pp. 59–129. Elsevier.

HIGUERA, F. J. 2004 Axisymmetric inviscid interaction of a bubble and a vortex ring. *Phys. Fluids* **16**, 1156–1159.

VAN DER HOEF, M. A., VAN SINT ANNALAND, M., DEEN, N. G. & KUIPERS, J. A. M. 2008 Numerical simulation of dense gas–solid fluidized beds: a multiscale modelling strategy. *Annu. Rev. Fluid Mech.* **40** (1), 47–70.

HSIAO, C.-T. & CHAHINE, G. 2004 Prediction of tip vortex cavitation inception using coupled spherical and nonspherical bubble models and Navier–Stokes computations. *J. Mar. Sci. Technol.* **8** (3), 99–108.

JACKSON, R. 1997 Locally averaged equations of motion for a mixture of identical spherical particles and a Newtonian fluid. *Chem. Engng Sci.* **52** (15), 2457–2469.

JAMES, S. & MADNIA, C. K. 1996 Direct numerical simulation of a laminar vortex ring. *Phys. Fluids* **8** (9), 2400–2414.

JOSEPH, D., LUNDGREN, T., JACKSON, R. & SAVILLE, D. 1990 Ensemble averaged and mixture theory equations for incompressible fluid particle suspensions. *Intl J. Multiphase Flow* **16** (1), 35–42.

KUIPERS, J. A. M., VAN DUIN, K. J., VAN BECKUM, F. P. H. & VAN SWAAIJ, W. P. M. 1993 Computer simulation of the hydrodynamics of a two-dimensional gas-fluidized bed. *Comput. Chem. Engng* **17** (8), 839–858.

LAIN, S. & GARCIA, J. A. 2006 Study of four-way coupling on turbulent particle-laden jet flows. *Chem. Engng Sci.* **61** (20), 6775–6785.

LI, Y., MCLAUGHLIN, J. B., KONTOMARIS, K. & PORTELA, L. 2001 Numerical simulation of particle-laden turbulent channel flow. *Phys. Fluids* **13** (10), 2957–2967.

LOHSE, D. & PROSPERETTI, A. 2003 Controlling bubbles. *J. Phys.: Condens. Matter* **15** (1), S415–S420.

MAGNAUDET, J. & EAMES, I. 2000 The motion of high-Reynolds-number bubbles in inhomogeneous flows. *Annu. Rev. Fluid Mech.* **32** (1), 659–708.

MAXEY, M. R. & RILEY, J. J. 1987 Gravitational settling of aerosol particles in homogeneous turbulence and random flow fields. *J. Fluid Mech.* **174** (1), 441–465.

MAXEY, M. R. 1983 Equation of motion for a small rigid sphere in a non-uniform flow. *Phys. Fluids* **26** (4), 883–889.

MAZZITELLI, I. & LOHSE, D. 2009 Evolution of energy in flow driven by rising bubbles. *Phys. Rev.* E **79** (6), 066317.

MAZZITELLI, I. M., LOHSE, D. & TOSCHI, F. 2003 The effect of microbubbles on developed turbulence. *Phys. Fluids* **15** (1), L5.

MERLE, A., LEGENDRE, D. & MAGNAUDET, J. 2005 Forces on a high-Reynolds-number spherical bubble in a turbulent flow. *J. Fluid Mech.* **532**, 53–62.

MITTAL, R., DONG, H., BOZKURTTAS, M., NAJJAR, F. M., VARGAS, A. & VON LOEBBECKE, A. 2008 A versatile sharp interface immersed boundary method for incompressible flows with complex boundaries. *J. Comput. Phys.* **227** (10), 4825–4852.

MOHSENI, K., RAN, H. & COLONIUS, T. 2001 Numerical experiments on vortex ring formation. *J. Fluid Mech.* **430**, 267–282.

MOIN, P. & APTE, S. V. 2006 Large-eddy simulation of realistic gas turbine combustors. *AIAA J. v44* **698**, 698–708.

ORMIÈRES, D. & PROVANSAL, M. 1999 Transition to turbulence in the wake of a sphere. *Phys. Rev. Lett.* **83** (1), 80–83.

OWEIS, G. F., VAN DER HOUT, I. E., IYER, C., TRYGGVASON, G. & CECCIO, S. L. 2005 Capture and inception of bubbles near line vortices. *Phys. Fluids* **17** (2), 022105.

RASTELLO, M., MARIÉ, J.-L., GROSJEAN, N. & LANCE, M. 2009 Drag and lift forces on interface-contaminated bubbles spinning in a rotating flow. *J. Fluid Mech.* **624** (1), 159–178.

RASTELLO, M., MARIÉ, J.-L. & LANCE, M. 2011 Drag and lift forces on clean spherical and ellipsoidal bubbles in a solid-body rotating flow. *J. Fluid Mech.* **682**, 434–459.

READE, W. C. & COLLINS, L. R. 2000 Effect of preferential concentration on turbulent collision rates. *Phys. Fluids* **12**, 2530.

ROUSON, D. W. I. & EATON, J. K. 2001 On the preferential concentration of solid particles in turbulent channel flow. *J. Fluid Mech.* **428** (1), 149–169.

SCHILLER, L. & NAUMANN, A. 1935 A drag coefficient correlation. *Z. Verein. Deutsch. Ing.* **77**, 318–320.

SEGURA, J. C., EATON, J. K. & OEFELEIN, J. C. 2004 Predictive capabilities of particle-laden large-eddy simulation. *Report No.* TSD-156, Department of Mechanical Engineering, Stanford University.

SHAMS, E. & APTE, S. V. 2010 Prediction of small-scale cavitation in a high speed flow over an open cavity using large-eddy simulation. *Trans. ASME: J. Fluids Engng* **132**, 111301.

SHAMS, E., FINN, J. & APTE, S. V. 2011 A numerical scheme for Euler–Lagrange simulation of bubbly flows in complex systems. *Intl J. Numer. Meth. Fluids* **67** (12), 1865–1898.

SOKOLICHIN, A., EIGENBERGER, G., LAPIN, A. & LUBERT, A. 1997 Dynamic numerical simulation of gas–liquid two-phase flows: Euler/Euler versus Euler/Lagrange. *Chem. Engng Sci.* **52** (4), 611–626.

SOMMERFELD, M., ANDO, A. & WENNERBERG, D. 1992 Swirling, particle-laden flows through a pipe expansion. *J. Fluids Engng* **114** (4), 648–656.

SOMMERFELD, M. & QIU, H. H. 1993 Characterization of particle-laden, confined swirling flows by phase-Doppler anemometry and numerical calculation. *Intl J. Multiphase Flow* **19** (6), 1093–1127.

SQUIRES, K. D. & EATON, J. K. 1991 Preferential concentration of particles by turbulence. *Phys. Fluids A: Fluid Dyn.* **3** (5), 1169.

SRIDHAR, G. & KATZ, J. 1995 Drag and lift forces on microscopic bubbles entrained by a vortex. *Phys. Fluids* **7** (2), 389.

SRIDHAR, G. & KATZ, J. 1999 Effect of entrained bubbles on the structure of vortex rings. *J. Fluid Mech.* **397**, 171–202.

TOMBOULIDES, A. G. & ORSZAG, S. A. 2000 Numerical investigation of transitional and weak turbulent flow past a sphere. *J. Fluid Mech.* **416** (1), 45–73.

VAN NIEROP, E. A., LUTHER, S., BLUEMINK, J. J., MAGNAUDET, J., PROSPERETTI, A. & LOHSE, D. 2007 Drag and lift forces on bubbles in a rotating flow. *J. Fluid Mech.* **571**, 439–454.

VREMAN, A. W. 2007 Turbulence characteristics of particle-laden pipe flow. *J. Fluid Mech.* **584**, 235–279.

WANG, Q. & SQUIRES, K. D. 1996 Large eddy simulation of particle-laden turbulent channel flow. *Phys. Fluids* **8**, 1207–1223.

XU, J., MAXEY, M. R. & KARNIADAKIS, G. E. 2002 Numerical simulation of turbulent drag reduction using micro-bubbles. *J. Fluid Mech.* **468** (1), 271–281.

YAMAMOTO, Y., POTTHOFF, M., TANAKA, T., KAJISHIMA, T. & TSUJI, Y. 2001 Large-eddy simulation of turbulent gas particle flow in a vertical channel: effect of considering inter-particle collisions. *J. Fluid Mech.* **442**, 303–334.

ZHANG, D. Z. & PROSPERETTI, A. 1997 Momentum and energy equations for disperse two-phase flows and their closure for dilute suspensions. *Intl J. Multiphase Flow* **23** (3), 425–453.